Wang *et al. Microstructures* **2025**, *5*, 2025066
DOI: 10.20517/microstructures.2024.117

Microstructures

Review

Open Access

Check for updates

Recent progress on synthesis and application of plasmonic metal heterostructures

Han Wang[1,2,#], Gina Jinna Chen[1,#], Biao Huang[3,#], Chenlong Xue[1], Jianlong Kuang[2], Longqing Cong[1], Perry Ping Shum[1,4], Yiyao Ge[2]

[1]State Key Laboratory of Optical Fiber and Cable Manufacture Technology, Guangdong Key Laboratory of Integrated Optoelectronics Intellisense, Department of EEE, Southern University of Science and Technology, Shenzhen 518055, Guangdong, China.
[2]State Key Laboratory for Advanced Metals and Materials, University of Science and Technology Beijing, Beijing 100083, China.
[3]Department of Materials Science and Engineering, National University of Singapore, Singapore 117575, Singapore.
[4]Pengcheng Laboratory, Shenzhen 518055, Guangdong, China.
[#]Authors contributed equally.

Correspondence to: Dr. Biao Huang, Department of Materials Science and Engineering, National University of Singapore, Singapore 117575, Singapore. E-mail: biaoh01@nus.edu.sg; Dr. Longqing Cong, State Key Laboratory of Optical Fiber and Cable Manufacture Technology, Guangdong Key Laboratory of Integrated Optoelectronics Intellisense, Department of EEE, Southern University of Science and Technology, No. 1088 Xueyuan Avenue, Shenzhen 518055, Guangdong, China. E-mail: conglq@sustech.edu.cn; Dr. Perry Ping Shum, State Key Laboratory of Optical Fiber and Cable Manufacture Technology, Guangdong Key Laboratory of Integrated Optoelectronics Intellisense, Department of EEE, Southern University of Science and Technology, No. 1088 Xueyuan Avenue, Shenzhen 518055, Guangdong, China; Pengcheng Laboratory, No. 2 Xingke 1st Street, Nanshan District, Shenzhen 518055, Guangdong, China. E-mail: shum@ieee.org; Dr. Yiyao Ge, State Key Laboratory for Advanced Metals and Materials, University of Science and Technology Beijing, No. 30 Xueyuan Road, Haidian District, Beijing 100083, China. E-mail: yiyaoge@ustb.edu.cn

How to cite this article: Wang, H.; Chen, G. J.; Huang, B.; Xue, C.; Kuang, J.; Cong, L.; Shum, P. P.; Ge, Y. Recent progress on synthesis and application of plasmonic metal heterostructures. *Microstructures* **2025**, *5*, 2025066. https://dx.doi.org/10.20517/microstructures.2024.117

Received: 12 Nov 2024 **First Decision:** 3 Dec 2024 **Revised:** 14 Dec 2024 **Accepted:** 17 Dec 2024 **Published:** 11 Jun 2025

Academic Editor: Zhanxi Fan **Copy Editor:** Fangling Lan **Production Editor:** Fangling Lan

Abstract

In the past decade, plasmonic metal heterostructures have been widely studied for their unique plasmon-enhanced effects and synergistic effects between different constituents. The intriguing properties of plasmonic metal heterostructures arise from the synergistic and/or complementary interactions of their components and the nanoscale interfaces between different materials. In addition, plasmonic metal heterostructures exhibit interesting optical and catalytic properties depending on their composition, shape, size, and architecture. This review provides an overview of the recent progress on the synthesis of plasmonic metal heterostructures including core-shell, core-satellites, Janus, and other typical structures, and then introduces some of the latest applications including surface-

enhanced Raman scattering, sensing, and electrocatalysis of these plasmonic metal heterostructures. Finally, the challenges and prospects for the development of novel high-performance plasmonic metal heterostructures in the future are presented.

Keywords: Plasmonic metals, heterostructures, metal nanomaterials

INTRODUCTION

Plasmonic metals have been extensively investigated due to their fascinating physicochemical properties, which enable a wide range of applications in fields such as catalysis[1-14], plasmonic solar cells[15-18], surface-enhanced Raman scattering (SERS)[19-22], and molecule detection[23-25]. In particular, plasmonic metals exhibit unique optical properties and demonstrate strong interactions with electromagnetic radiation such as photons, which is achieved through the excitation of localized surface plasmon resonance (LSPR)[26]. For example, gold (Au), silver (Ag), and copper (Cu) nanostructures display resonance phenomena when interacting with ultraviolet and visible photons, resulting in significant optical characteristics in these wavelength ranges[27]. Consequently, the unique interactions and properties of plasmonic metals have led to significant interest in their potential applications.

The rational design and controlled construction of metal heterostructures offer a promising approach to developing novel materials with unique properties and enhanced performance in various applications[28]. Compared to single-component nanomaterials, metal heterostructures that consist of two different metal elements can also combine the superior properties of their different components, making them more attractive for various applications[29-33]. Notably, due to the synergistic effects and/or complementary actions between different components[34], plasmonic metal heterostructures may exhibit unique functionalities and properties, such as distinct plasmonic effects different from the individuals, and can be designed with well-defined structures, which have great potential for applications in fields such as optoelectronics[35], energy conversion[36], and catalysis[37]. Therefore, constructing plasmonic metal heterostructures has grabbed increasing research interest.

Significant progress has been made in the preparation and application of plasmonic metal heterostructures in the past decade. In this review, we first introduce the properties of typical plasmonic metals (Au, Ag, and Cu) and their unique plasmonic characteristics. Then, we summarize the synthesis strategies for the preparation of various types of plasmonic metal heterostructures composed of different metals with distinct architectures, including core-shell, core-satellites, and Janus structures. The practical applications of these plasmonic heterostructures in SERS, sensing, and electrocatalysis will also be demonstrated. Finally, we will summarize and discuss the challenges and future direction in this emerging research area.

PROPERTIES OF PLASMONIC METALS

The plasmonic and optical properties of nanoparticles depend on the intrinsic dielectric function of the metal[38]. In the visible light range, Au and Ag exhibit excellent plasmonic performance, offering a high-quality factor[39]. Ag nanoparticles (Ag NPs) possess outstanding plasmonic properties at wavelengths above 320 nm, resonating effectively across the visible light range, which is primarily due to a negative real part of the dielectric function and a small imaginary part[40]. In contrast, Au displays effective plasmonic properties within the 500 to 800 nm range. However, for wavelengths below 500 nm, Au nanoparticles (Au NPs) undergo interband transitions, leading to greater absorption losses and a reduced plasmonic response in this wavelength range[38]. Compared to the extensively studied noble metal materials such as Ag and Au, some non-noble plasmonic metals can also demonstrate good performance across the spectrum and are more

cost-effective. For instance, aluminum (Al) and Cu exhibit excellent plasmonic properties in the ultraviolet-visible-near-infrared spectrum. As a result, these materials are gaining increasing attention in this field[41-44]. We will give a detailed description of the typical plasmonic metals, i.e., Au, Ag, and Cu, as follows.

Au nanocrystals have been widely applied in fields such as catalysis and optics[45-50], with their physicochemical properties tunable by size and shape[51]. The size and shape of Au NPs also determine the properties of surface plasmon resonance (SPR), which directly affects their optical absorption and scattering characteristics[52,53]. During synthesis, the shape and size of Au nanomaterials can be precisely controlled by altering the reaction conditions, which provides a great platform for tuning their properties. It has also been found that the shape and size of Au nanomaterials can affect their electronic structures, including band structure and electronic transport properties[54], thus determining their performances in diverse applications such as catalysis. It is also worth mentioning that Au nanomaterials exhibit excellent chemical inertness and biocompatibility, broadening their applications[55].

Ag nanomaterials also possess unique optical and electrical properties[56,57]. In SERS technology, Ag NPs could exhibit more than 100 times the enhancement compared to Au NPs with similar structures[58], which suggests the superior LSPR properties of Ag nanomaterials. Additionally, Ag NPs exhibit exceptional antibacterial properties[59]. Despite the outstanding plasmonic performance of Ag in the visible light range and its widespread use in optical applications, Ag nanomaterials face limitations due to their instability under environmental conditions, such as oxidation, and their inherent toxicity[60]. Furthermore, it remains a great challenge to achieve the preparation of Ag nanomaterials with uniform size, controllable morphology and high purity[53].

Cu is a widely available and relatively inexpensive metal, with its nanocrystals demonstrating significant potential in various fields, including plasmonics[61,62], catalysis[63,64], and electronics[65]. For example, it can exhibit optical enhancement effects in optical applications, particularly within the visible to near-infrared spectrum. Cu also shows great potential for application in electrochemical reactions including the electrochemical conversion of carbon dioxide (CO_2) into molecules containing two or more carbon atoms (i.e., C_{2+} products)[66-70]. Therefore, the research and development of Cu-based electrocatalysts are of great importance for the chemical industry and sustainable energy[37]. However, there is still a lack of effective methods for synthesizing Cu nanomaterials, especially those with precise sizes and shapes. Besides, the chemical instability further limits the widespread practical use of Cu and Cu-based materials.

SYNTHESIS OF PLASMONIC METAL HETEROSTRUCTURES

Core-shell heterostructure

Core-shell structured metal heterostructures represent a versatile class of nanomaterials that combine distinct properties of different metals to achieve enhanced performances or new functions. In these structures, a core of one metal is enveloped by a shell of another, enabling the integration of their unique properties. Besides, the ability to fine-tune the core and shell materials, along with their respective thicknesses during the synthesis, provides a great platform to optimize their performance for specific applications[71]. Seeded-mediated methods are commonly used to prepare core-shell metal heterostructure. During the synthesis, metal seeds with different sizes and morphologies are first prepared as the core material and dispersed in a solvent, followed by the reduction of metal precursor and the deposition of secondary metal as the shell, whose growth could be controlled by tuning the reaction conditions such as the concentration of metal precursor, the shape of the metal seeds, the reductant, temperature, time and pH of the solution.

Typically, Au nanomaterials are frequently used as the core material due to their high stability, uniform size, and tunable morphology, and Ag shells could be easily grown on Au core due to their small lattice mismatch. In a typical work, spiky Au NPs were first prepared as the seed[72]. Then, the Ag shell was *in situ* deposited on the surface of these Au cores by polyol process under high-temperature conditions to form Au@Ag core-shell spiky nanomaterials with adjustable size. It is worth noting that the thickness of the Ag shell could be controlled by tuning the added amount of Ag precursor ($AgNO_3$). In the design of Au@Ag bimetallic core-shell nanostructures, the core's geometry significantly influences the final morphology of the nanomaterials and Ag coating. In a typical work, Qi *et al.* successfully synthesized Au nanobipyramids-Ag core-shell (Au NBs@Ag) nanomaterials and Au nanorods-Ag core-shell (Au NRs@Ag) nanomaterials by seed-mediated growth method using Au NBs and Au NRs as the seed[73]. It is noteworthy that two distinct Ag deposition processes were found on different Au seeds. Specifically, the shape of Au NBs changed from bipyramid to rice, and finally cylindrical rod, while Au NRs gradually changed from nanorod shape to spherical, triangular pyramid, octahedron, and other irregular forms. It is worth noting that the volume of the Au NBs seed solution affects the aspect ratios of Au NBs@Ag and the shape of its tip. When the seed solution was used in small quantities, it would give Au NBs@Ag a sharp tip. When a large amount of seed solution was used, the sharp edges would disappear. Self-assembled Au nanostructure could also be used as the seed for the growth of Ag to form core-shell heterostructure. In a typical work, Tanwar *et al.* first synthesized Au nanorods through seed-mediated growth and then self-assembled them into vertical arrays[35]. By epitaxial growth of Ag on pre-assembled Au nanorods, a self-assembled bimetallic Au-Ag nanorods vertical array was finally obtained, and the precise regulation of the distance between Au and Ag was realized [Figure 1A].

Cu can also be deposited on Au to form a core-shell structure by fine-tuning the reaction process with the assistance of appropriate ligand, despite the large lattice mismatch between the two metals. For instance, Hsia *et al.* synthesized Au-Cu core-shell nanocubes [Figure 1B] and octahedra [Figure 1C] by aqueous-phase synthesis[74]. In this process, octahedral Au nanocrystals were first synthesized using a hydrothermal method and used as the seed for the growth of Cu. Then, Cu precursor was reduced at high temperatures using ascorbic acid as the reducing agent in the presence of hexadecylamine (HDA), Au-Cu core-shell nanocubes and Au-Cu core-shell octahedras were synthesized by using $CuCl_2$ and Cu $(CH_3COO)_2$ as the Cu precursor, respectively. In the end, Au-Cu core-shell nanocubes with adjustable edge lengths and octahedra with different opposite corner distances were formed. During synthesis, the addition of HDA increased the pH of the solution, and also acted as the coordinating ligand of Cu ions to promote the controlled growth of Cu shells. However, the large lattice mismatch between Au and Cu led to uneven Cu deposition, causing the Au cores in Au-Cu core-shell nanocubes and octahedrons to shift from a central position. In another work, Lyu *et al.* synthesized Au@Cu core-shell nanocubes using a seed-mediated growth method[75], which employed glucose as a reducing agent, with HDA and chloride ion serving as capping agents for the Cu {100} crystal face. The thickness of the Cu shell was controlled by changing the reaction time and/or the concentration of Au seeds. A longer reaction time or a higher concentration of Au seeds would lead to a decreased thickness of the Cu shell, and Au@Cu nanocubes with adjustable size ranging from 20 and 30 nm were obtained [Figure 1D]. Notably, the distribution of Au cores was random due to a 12% large lattice mismatch between Au and Cu, resulting in local epitaxial growth of Cu shells on Au seeds. The elemental distribution of the core (Au, green) and shell (Cu, red) could be clearly observed in the energy-dispersive X-ray (EDX) mapping [Figure 1E].

In addition to Au nanomaterials, Ag nanomaterials with various morphologies can also serve as the core for the growth of other plasmonic metals, forming core-shell heterostructures. For instance, Ag nanowires could be prepared using the polyol method as a template[76]. Subsequently, core-shell Ag@Au nanowires

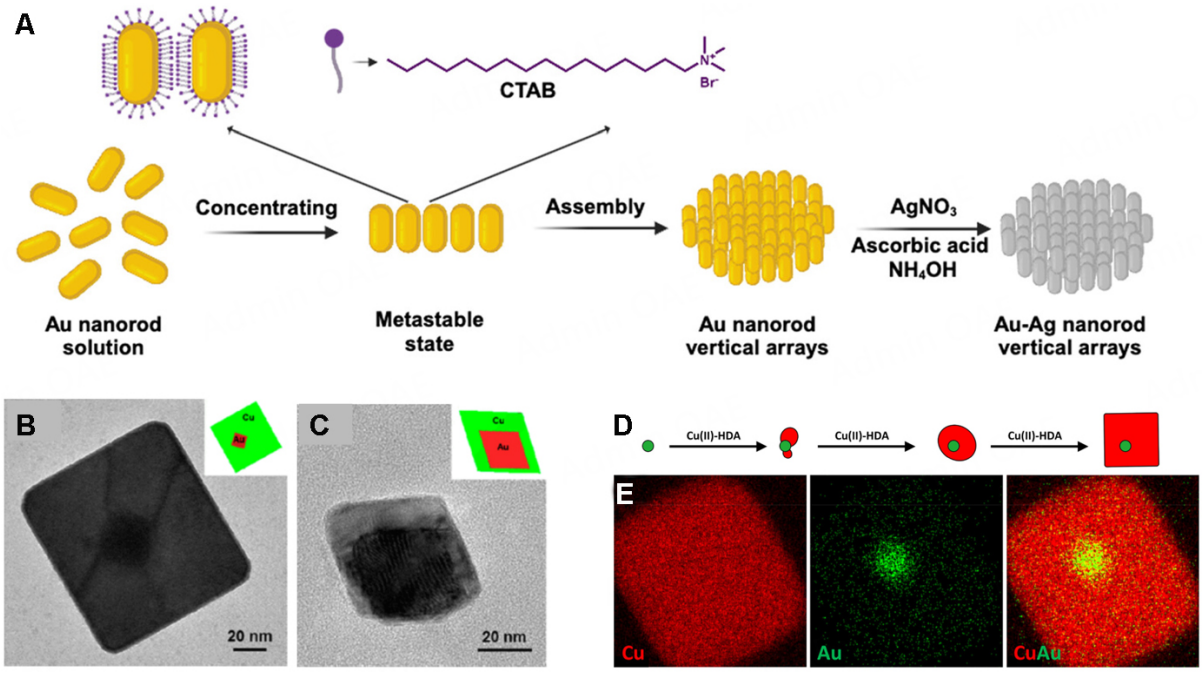

Figure 1. (A) Schematic illustration of the fabrication of an Au-Ag nanorod array[35]. TEM image with a schematic illustration of the structure of (B) Au-Cu core-shell nanocubes and (C) Au-Cu core-shell octahedra[74]. (D) Schematic illustration of the synthesis of Au@Cu nanocubes and (E) EDX mapping of Au@Cu core-shell nanocubes[75].

were prepared by the deposition of Au shell onto the Ag core. These Ag@Au nanowires could then be welded together through mixed vapor-induced capillary force, forming stretchable and transparent electrodes. In another work, Zhong *et al.* prepared Ag@Cu core-shell catalysts with Ag cores and porous Cu shells using Ostwald ripening and *in situ* electrochemical reduction techniques [Figure 2A][77]. By controlling the ripening time, three types of Ag@Cu catalysts with different pore sizes of the Cu shell were obtained, namely Ag@Cu-p2.8 (mean pore size of 2.8 nm), Ag@Cu-p4.9 (mean pore size of 4.9 nm) and Ag@Cu-p11.2 (mean pore size of 11.2 nm) with the transmission electron microscopy (TEM) images shown in Figure 2B-D.

Cu is less used as the core material due to the easy oxidation during the reaction. Zhang *et al.* synthesized Cu@Ag core-shell nanoparticles by a seed-mediated method[78]. Specifically, Cu nanoparticles were first synthesized and used as seeds for the subsequent deposition of Ag. The thickness of the Ag shell could be adjusted by varying the amount of Ag precursor. One key challenge in preparing Cu-based heterostructure is to prevent the oxidation of Cu during the reaction. To address this issue, Kuhn *et al.* developed a one-pot method involving sequential synthesis in a flowing CO atmosphere, in which Cu nanoparticles were first synthesized as the core, and the Ag shell was subsequently grown on the Cu core by directly injecting Ag precursor into the solution [Figure 2E][37]. During the reaction, the thickness of the Ag shell could be controlled by adjusting the reaction time. With a longer reaction time, the thickness of the Ag shell could be increased, which ranged from a sub-atomic monolayer to several atomic layers.

Core-satellite heterostructures

Core-satellite structured metal heterostructures comprise a central core particle surrounded by multiple smaller satellite particles. This unique architecture allows for enhanced surface area and increased interactions between the core and satellites, resulting in improved optical, electronic, and catalytic

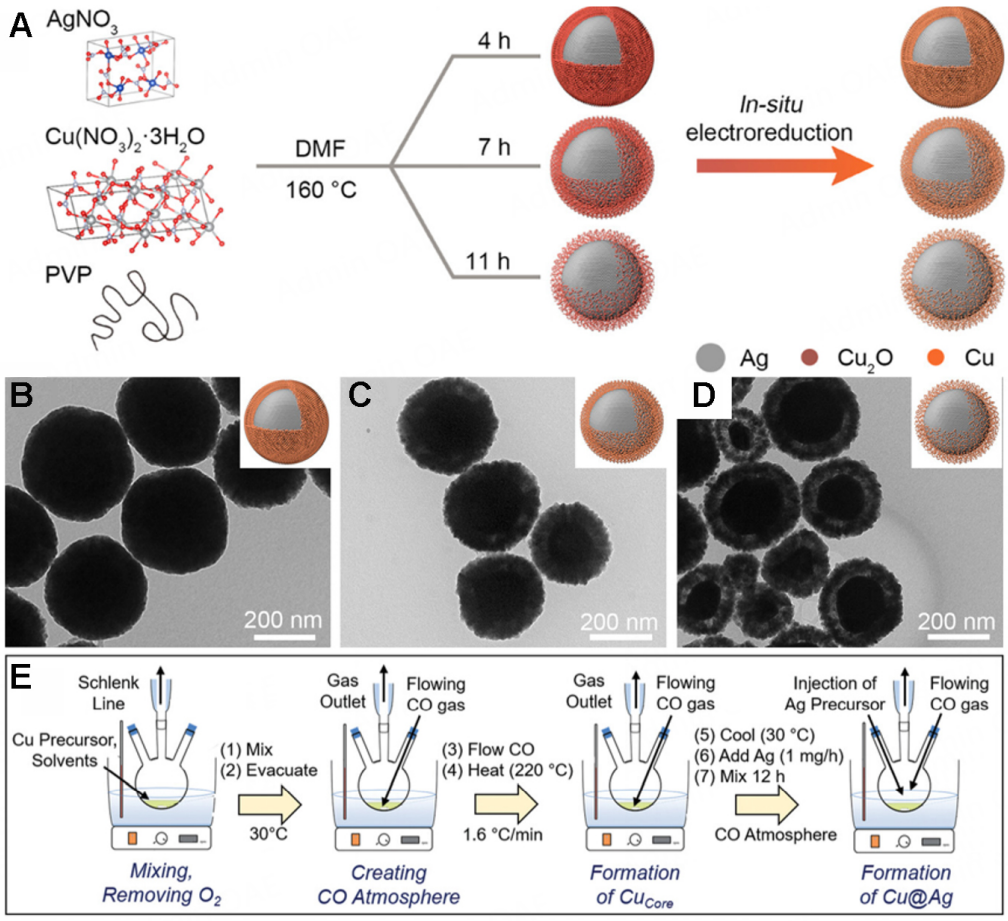

Figure 2. (A) Schematic illustration of the synthesis of three types of Ag@Cu heterostructures, (B-D) TEM images of Ag@Cu-p2.8 (B), Ag@Cu-p4.9 (C), and Ag@Cu-p11.2 (D)[77]. (E) Schematic illustration of the synthesis process of Cu@Ag core-shell nanoparticles[37].

properties[79]. Typically, the synthesis of core-satellite heterostructures begins with the preparation of the metal core, followed by the deposition of smaller satellites through the reduction of a metal precursor in a seed solution. To obtain core-satellite instead of core-shell heterostructure, the reduction and deposition of the shell on the metal core should be modulated by controlling factors such as reaction conditions, ligand selection, and surface properties of the seed. For example, lower metal precursor concentrations or faster reaction kinetics typically result in the formation of core-satellite heterostructures. In contrast, slower reaction kinetics or the use of ligands that strongly bond to the metal core surface can promote the growth of a continuous shell, resulting in a core-shell morphology.

In a typical study, core-satellite Au-Ag nanoparticles were synthesized by seed-mediated growth method using Au NPs as the seed[80]. It is worth noting that core-shell Au-Ag heterostructures could be obtained using the same seed-mediated method except for increasing the concentration of Ag precursor. During the growth, the size of the resultant core-satellite Au-Ag nanoparticles could be controlled by changing the added amount of Ag precursor ($AgNO_3$) or the Au seeds in the solution. Furthermore, a one-dimensional nanochain was then generated by self-assembly of the obtained core-satellite Au-Ag nanoparticles [Figure 3A], with the TEM image shown in Figure 3B.

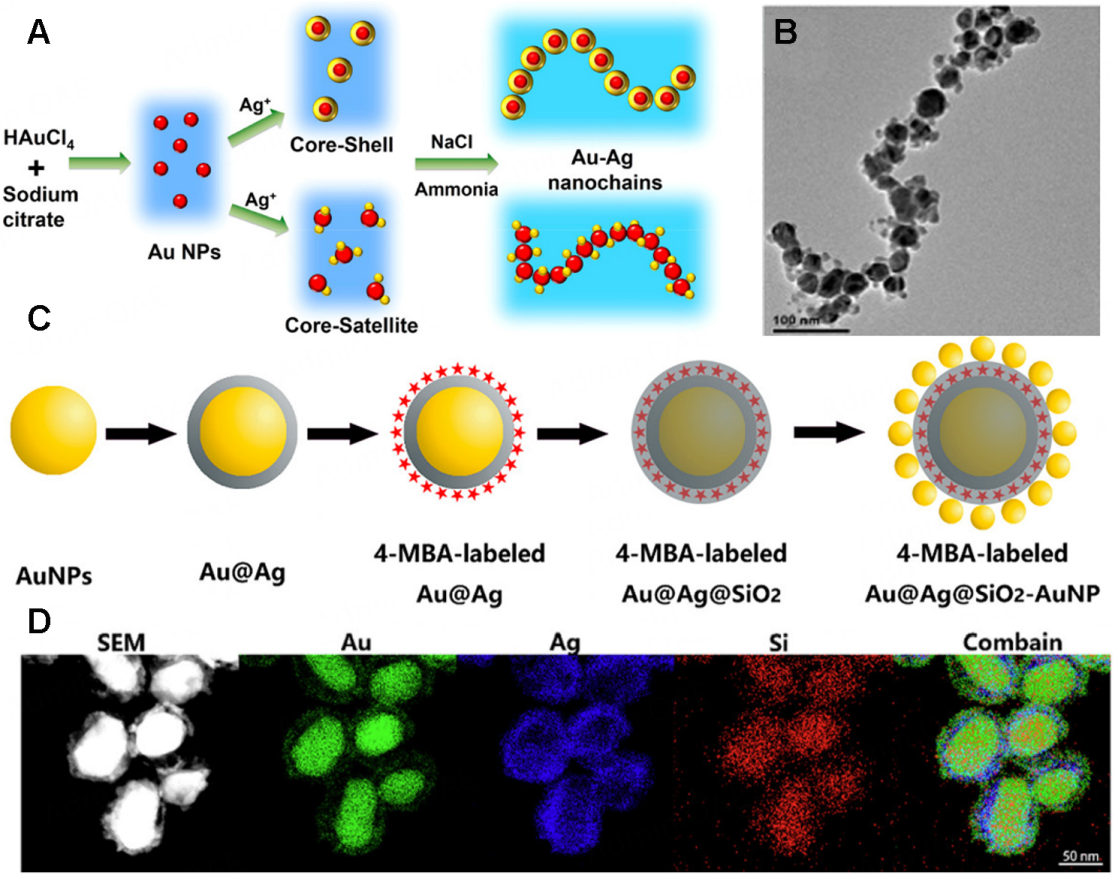

Figure 3. (A) Schematic illustration of the formation of Au-Ag nanochains by the assembly of hybrid Au-Ag nanoparticles and (B) TEM image of Au-Ag nanochains assembled by core-satellite Au-Ag nanoparticles[80]. (C) Schematic illustration of the synthesis and (D) EDS elemental mapping of Au@Ag@SiO_2-AuNP nanoassemblies labeled with 4-MBA[81].

The core-shell-satellite structure extends the core-satellite design by adding an intermediate layer (usually silica, SiO_2) between the core and satellite particles. This SiO_2 interlayer enhances water solubility of the core-shell-satellite structure compared to the core-satellite structure and ensures that the satellite particles are uniformly distributed across the silica surface, effectively preventing nanoparticle aggregation. For example, Yang *et al.* prepared multilayer Au@Ag@SiO_2-AuNP core-shell-satellite nanostructures by layer-by-layer deposition [Figure 3C][81]. First, Au nanospheres were synthesized and coated with a layer of Ag to form Au@Ag core-shell heterostructure. Subsequently, 4-mercaptobenzoic acid (4-MBA) was attached to the Au@Ag surface to facilitate the growth of a SiO_2 layer. In addition, (3-aminopropyl) trimethoxysilane (APTMS) was used to introduce amine functionality on the surface to modify Au@Ag@SiO_2. Finally, Au nanosphere satellites were grown on the surface of Au@Ag@SiO_2 by seed-mediated method by rapid reduction of Au salt with a strong reductant ($NaBH_4$) to obtain Au@Ag@SiO_2-AuNP heterostructure. The number of Au satellites could be increased by adding more Au salt. Energy dispersive X-ray spectroscopy (EDS) elemental mapping [Figure 3D] confirms the formation of the 4-MBA-labeled Au@Ag@SiO_2-AuNP nanoassemblies.

Janus heterostructures

The term "Janus" originates from Roman mythology, referring to the god of gates, who is depicted with two faces looking in opposite directions[82]. Janus particles are nano- or microscale particles with two distinct chemical or surface compositions. In recent years, Janus nanoparticles have garnered considerable attention

due to their unique properties and diverse applications in fields such as SERS detection[83], catalysis[84], and biosensing[85]. For the synthesis of Janus heterostructures, the key is to achieve the asymmetric growth of the metal on the pre-synthesized seeds. Several strategies could be applied to achieve the preparation of Janus metal heterostructures, such as template-assisted growth, surface functionalization of the seed with specific ligands or surfactants, manipulation of the reaction kinetics, and usage of lattice mismatch between the metal seed and secondary metal.

Janus heterostructures can be prepared by partially coating the seed with the inert material, followed by the deposition of secondary metals on the uncoated sites and the subsequent removal of the inert materials. For example, Qiu *et al.* proposed a general method for synthesizing Janus heterodimers of metal nanoparticles using Au NPs as the seed[86]. In this approach, the surface of Au NPs was partially covered with polystyrene (PS). The presence of Au NPs during styrene polymerization affected the growth pattern of PS, limiting its growth to one side of the Au NPs [Figure 4A]. Then, the unoccupied surface of Au NPs served as the active site for the heterogeneous nucleation and growth of Ag NPs, thus promoting the asymmetric growth of Ag in the dimer structure and forming PS-Au-Ag colloidal particles. Finally, PS was removed by tetrahydrofuran (THF) to obtain Au-Ag Janus heterodimers. It is worth noting that the contact area between the two metal nanoparticles could be adjusted by controlling the exposed area on the surface of the Au NPs after coverage of PS. The TEM image [Figure 4B] clearly showed the formation of Janus heterostructure, while the EDX mapping showed the spatial separation between Au and Ag [Figure 4C]. In another work, Feng *et al.* introduced a stepwise seeded growth method for synthesizing rod-shaped plasmonic metal nanostructures[87]. As shown in Figure 4D, Au NPs were first deposited on the surface of SiO_2 spheres, followed by the deposition of an additional SiO_2 layer onto the resulting SiO_2-Au structure. Due to the different chemical properties of Au and SiO_2, the affinity of SiO_2 for itself is greater than that for Au. Taking advantage of this difference, the additional SiO_2 layer was preferentially deposited on the surface of the SiO_2 substrate in SiO_2-Au@SiO_2 nanostructure, in which part of Au NPs near the attachment point was embedded into the additional SiO_2 layer, while the other part of AuNPs was exposed. Next, other metal components such as Ag NPs were grown on the exposed surface of Au NPs to form a Janus heterodimer. It is worth noting that the ratio of the exposed surface of Au seeds during seed growth depends on the thickness of the additional SiO_2 layer [Figure 4E], which led to the formation of three types of Au-Ag Janus heterodimers [Figure 4F].

The use of appropriate ligands is another effective approach to achieve the synthesis of Janus metal heterostructures, which modulate the surface energy and provide selective growth sites on the metal seeds, enabling localized deposition of the secondary metal. In a typical work, Wang *et al.* synthesized Au-Ag Janus nanoparticles using a seed-mediated growth method with Au NPs as the seed[88]. Specifically, 2-mercaptobenzoimidazole-5-carboxylic acid (MBIA) was used to modify Au NPs and regulate the metal-metal interfacial energy between Au and Ag, thereby guiding the directional deposition of Ag islands. Hydroquinone (HQ) served as the reducing agent to reduce $AgNO_3$, form Ag islands over the Au NPs and resulted in anisotropic Au-Ag Janus nanoparticles with good dispersion and uniform morphology. Xu *et al.* further grew Au spots on the surface of Au-Ag Janus nanoparticles to form Au-Ag Janus@Au NPs[89]. Notably, the structure of Au-Ag Janus@Au NPs could be tuned by altering the pH of the solution, leveraging the galvanic replacement reaction between $HAuCl_4$ and Ag islands [Figure 4G]. Hollow Au-Ag Janus@Au NPs (denoted as Au-Ag Janus@Au(hollow) NPs) were produced at a pH range of 3.0-5.0, while solid Au-Ag Janus@Au NPs (denoted as Au-Ag Janus@Au(solid) NPs) formed under a pH range of 7.0-9.5. It was reported that the formation of Au-Ag Janus@Au(solid) NPs was attributed to the strong reducing capability of ascorbic acid under specific alkaline conditions, which preferentially reduced $HAuCl_4$ and inhibited the galvanic replacement reaction. The scanning TEM (STEM) image and element mapping in

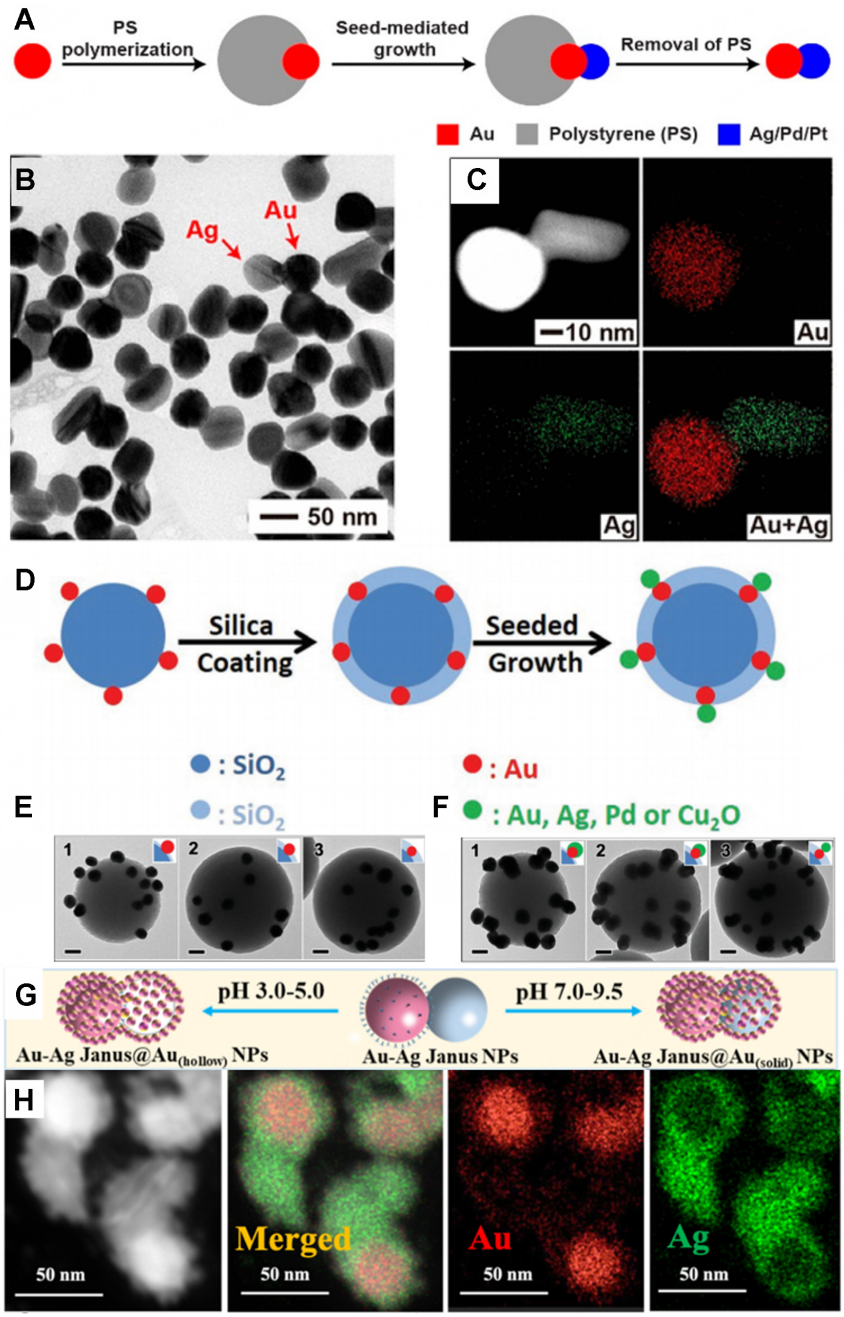

Figure 4. (A) Schematic illustration of the synthesis of Janus heterodimers, (B) TEM image of Au-Ag Janus dimers and (C) STEM image with elemental mapping of an induvial Au-Ag Janus dimer[86]. (D) Schematic illustration of the synthesis of Janus dimer on the surface of SiO_2 spheres, (E) TEM images with the structural model in the inset of SiO_2-Au@SiO_2 with different layer thicknesses of the additional SiO_2 layer and (F) TEM images with the structural model in the inset of SiO_2-Au dimers after growth of Au. The scale bars in (G and H) are 50 nm[87]. (G) Schematic illustration of the synthesis of Au-Ag Janus@Au (solid) NPs and Au-Ag Janus@Au (hollow) NPs under different pH conditions and (H) STEM image with elemental mapping of Au-Ag Janus@Au (solid) nanoparticles[89].

Figure 4H clearly revealed the distribution of Au and Ag elements within the Au-Ag Janus@Au(solid) NPs, further confirming the formation of the Au-Ag Janus structure. Moreover, the growth of numerous Au dots could also be observed on the surface of Au-Ag Janus nanoparticles. In another work, Zeng *et al.* proposed a novel seed-mediated strategy for the construction of Au-Ag Janus metal heterostructure by modulating the

atomic absorption energy on the surface of the Au seed[90]. Ag atoms were preferentially deposited in areas with lower atomic absorption energy for further growth, achieving continuous tunability of the contact area between Au and Ag and the number/size of Ag islands on Au seeds within the same system. During the reaction, the surface of the Au seeds was first modified with two ligands including poly(-diallyldimethylammonium) chloride (PDDA) and fish sperm DNA (FSDNA). Due to the higher atomic adsorption energy on the FSDNA-modified Au surface than that on the PDDA-modified Au surface, Ag atoms deposited and grew preferentially on the PDDA-rich areas of the Au sphere surface to achieve the preparation of Janus Au-Ag heterostructure. In another work, Wu *et al.* synthesized various Au-Ag hybrid nanoparticles, including core-shell, Janus, and core-satellite structures by controlling the amounts of MBIA, $AgNO_3$, or HQ added[91]. As the volume of $AgNO_3$ increased, the morphology of the Au-Ag hybrid nanoparticles changed from Janus structure to core-satellite structure. This change occurred because the concentration of $AgNO_3$ affected the distribution and deposition rate of Ag, which in turn influenced the morphology of nanoparticles. Similarly, the distribution and adsorption of MBIA molecules on the surface of Au NPs affect the amount and deposition locations of Ag, thus regulating the morphology of nanoparticles. The increased MBIA concentration led to a transition from core-shell to Janus and then to core-satellite structures of the Au-Ag hybrid nanoparticles. Besides Au-Ag Janus heterostructures, Au-Cu Janus heterostructures could also be prepared by choosing a suitable ligand to influence the interfacial energy between Au and Cu. Fan *et al.* developed a ligand-assisted seed-mediated method to prepare the Au-Cu Janus heterostructure, which achieved the island growth of Cu on Au seeds by introducing a strong thiol ligand to increase the interfacial energy between Au seeds and Cu domain[92]. Besides, the degree of asymmetry of the Au-Cu could be continuously tuned by modulating the amount of thiol ligand adsorbed on Au seeds. More interestingly, this method could be extended to Au seeds with different morphologies, including Au nanosphere, nanorod, and nanoplate. Zhang *et al.* proposed a semi-affinity strategy based on a seed-mediated method using the Au nanosphere as the seed[93]. Specifically, the seed-mediated synthesis of uniformly distributed Au-Cu heterostructures (Au-Cu HSs) with a continuously tuned interface was performed with the assistance of 1-hexadecylamine (HDA) and PDDA [Figure 5A]. By using HDA as the surfactant, the coverage of the Au-Cu interface was continuously adjusted to form a series of structurally adjustable Au-Cu cascade catalysts ranging from Au-Cu dimer (Au-Cu_I, Figure 5B) and Janus structures (Au-Cu_{II}, Figure 5C) to acorn-like Janus structure (Au-Cu_{III}, Figure 5D) and core-shell structures (Au-Cu_{IV}, Figure 5E).

Controlling the reaction kinetics by rationally tuning the experimental parameters such as the injection rate of metal precursors, type of metal precursors, and the strength of reducing agents can limit the speed of deposition of the secondary metals on the seed during the seed-mediated growth, thus facilitating the formation of Janus heterostructures. For example, Huang *et al.* employed a seeded-mediated approach to synthesize Ag-Cu nanodimers (NDs) with a tunable size of the Cu domain [Figure 5F][94]. The size of Cu domains on Ag NPs was controlled by using different Cu precursors and reducing agents to control the reaction kinetics during the overgrowth of Cu. The TEM image [Figure 5G] of the obtained Ag_I-$Cu_{1.1}$ (The mass ratio of Ag to Cu is 1:1.1) confirmed its typical Janus dimer structure. The X-ray Diffraction (XRD) pattern [Figure 5H] showed two sets of diffraction peaks corresponding to Ag and Cu, indicating the elemental separation of Cu and Ag within the dimer nanocrystals. Usually, syringe pumps can be used for the slow injection of the metal precursor and/or the reductant to lower the reaction kinetics. For example, Ma *et al.* synthesized three types of Ag-Cu Janus nanostructures with exposed {100} facets (JNS-100) and different atomic ratios between Ag and Cu by growing Cu on pre-synthesized Ag nanocubes[95]. The Janus structure was formed by precisely controlling the reaction kinetics using a syringe pump. The growth of Cu domains with different sizes was effectively restricted to the {100} face of one of the six equivalent faces of the Ag NCs by adjusting the reduction kinetics of surfactants and Cu precursors [Figure 6A]. The high-angle annular dark-field (HAADF-STEM) image [Figure 6B-D] and the corresponding EDS element

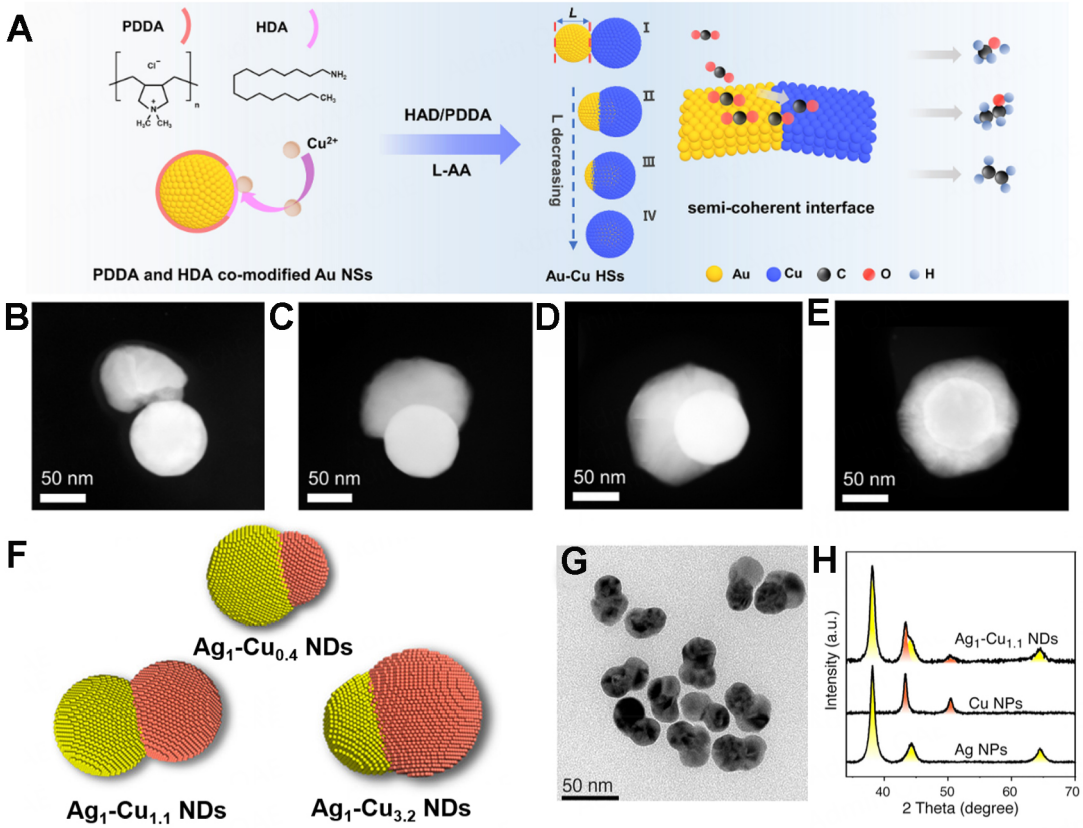

Figure 5. (A) Schematic illustration of the synthesis of distinct Au-Cu Janus heterostructures. (B-E) STEM images of different Au-Cu Janus heterostructures: (B) Au-Cu_I, (C) Au-Cu_{II}, (D) Au-Cu_{III}, and (E) Au-Cu_{IV}[93]. (F) Structural models of Ag-Cu Janus heterostructures with different ratios of the Cu domain, (G) TEM image, and (H) XRD pattern of Ag_1-$Cu_{1.1}$ NDs[94].

mapping [Figure 6E-G] clearly indicated the formation of Ag-Cu Janus heterostructures with different sizes of the Cu domains.

APPLICATIONS OF PLASMONIC METAL HETEROSTRUCTURES

Surface-enhanced Raman scattering

Surface-enhanced Raman scattering (SERS) was first observed in 1,974 with pyridine adsorbed on a rough Ag electrode[96]. This technique is widely utilized across various fields due to its ability to provide molecular fingerprint information[97-99], enable non-invasive detection[100-102], and achieve high sensitivity[103,104]. The SERS performance of metal nanoparticles is closely linked to their LSPR[105,106]. Key factors influencing the local electric field strength and SERS effectiveness include the nanoparticle edges' sharpness, nanoscale gaps, and surface roughness[107]. Precise control over the shape and growth of individual components is essential for enhancing SERS performance.

Plasmonic metal heterostructures have emerged as a transformative platform for SERS, significantly amplifying the sensitivity and specificity of molecular detection[71]. By integrating different metals, these heterostructures create intricate plasmonic landscapes that enhance localized electromagnetic fields, which are crucial for boosting the Raman signal of nearby molecules[108]. This approach also allows for fine-tuning of plasmonic properties, enabling optimized SERS performance across various wavelengths and enhancing the detection limits. Additionally, the versatility in designing these heterostructures opens new avenues for tailoring sensor properties. Du *et al.* utilized Au nanodumbbells (Au NDs) as seeds and varied the

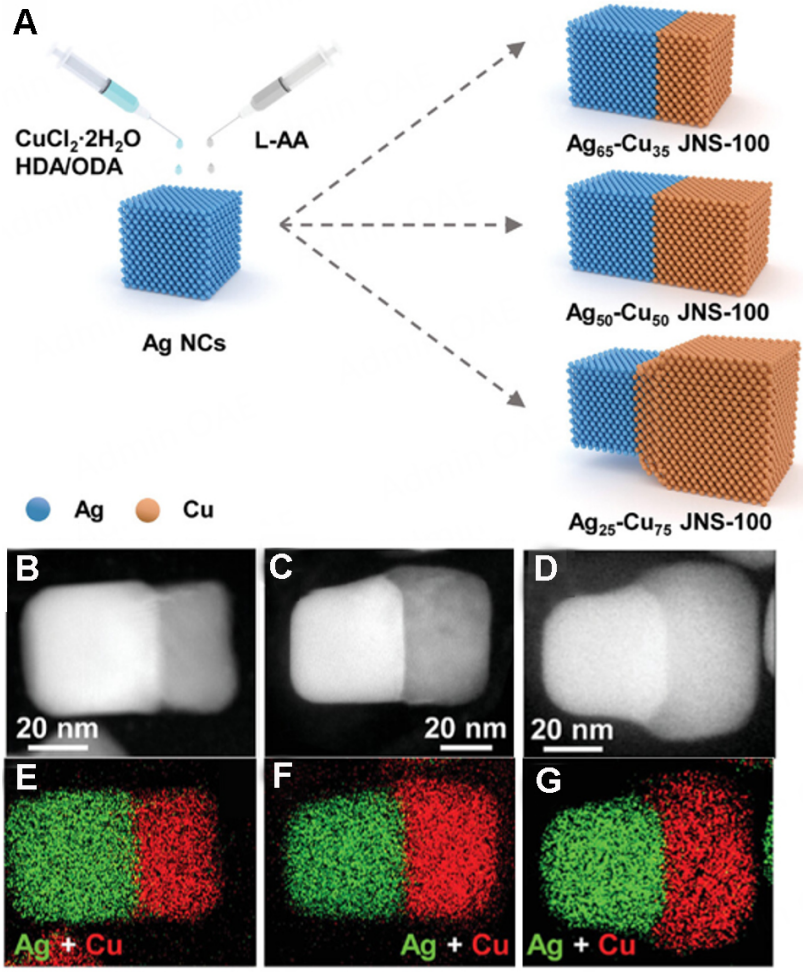

Figure 6. (A) Schematic of the synthesis of Ag-Cu JNS-100 Janus heterostructures and (B-G) HAADF-STEM images and EDS elemental mapping of different Ag-Cu JNS-100 Janus heterostructures: Ag_{65}-Cu_{35} JNS-100 (B, E), Ag_{50}-Cu_{50} JNS-100 (C, F), and Ag_{25}-Cu_{75} JNS-100 (D, G)[95].

concentration of 4-MBA in the growth solution, synthesizing a series of Au NDs@Ag NPs with diverse morphologies, including dumbbell-like core-shell structures, L-shaped Janus structures, and rod-like core-shell configurations[109]. Among these, the L-shaped Janus Au NDs@Ag NPs demonstrated the highest SERS enhancement factor (EF) of 1.41×10^7, which was attributed to the adjustable negative curvature and Ag deposition that generate sufficient hot spots. Arrays of ordered plasmonic nanoparticles are in high demand for optical sensing applications due to their ability to generate uniformly distributed plasmonic hotspots. This uniformity arises from their periodic structure and the effects of near-field coupling. For example, Tanwar *et al.* successfully designed a self-assembled vertical array of bimetallic Au-Ag nanorods[35]. At the characteristic peak of 1,070 cm^{-1}, the SERS signal intensity of 1 μM 4-MBA on the vertical array of Au-Ag nanorods was about five times higher than that of the monometallic Au nanorods array [Figure 7A and B]. It was found that this structure exhibited uniformly distributed plasma hot spots, which tightly confined the hot spots within the gaps between particles and created an enhanced electric field.

The stability and anti-oxidation properties of the substrate are crucial for the overall SERS performance. For instance, Feng *et al.* prepared two types of nanoparticles: Au-Ag Janus@Au(hollow) NPs and Au-Ag Janus@Au(solid) NPs[87]. The SERS signal from Au-Ag Janus@Au (solid) NPs was enhanced by a factor of

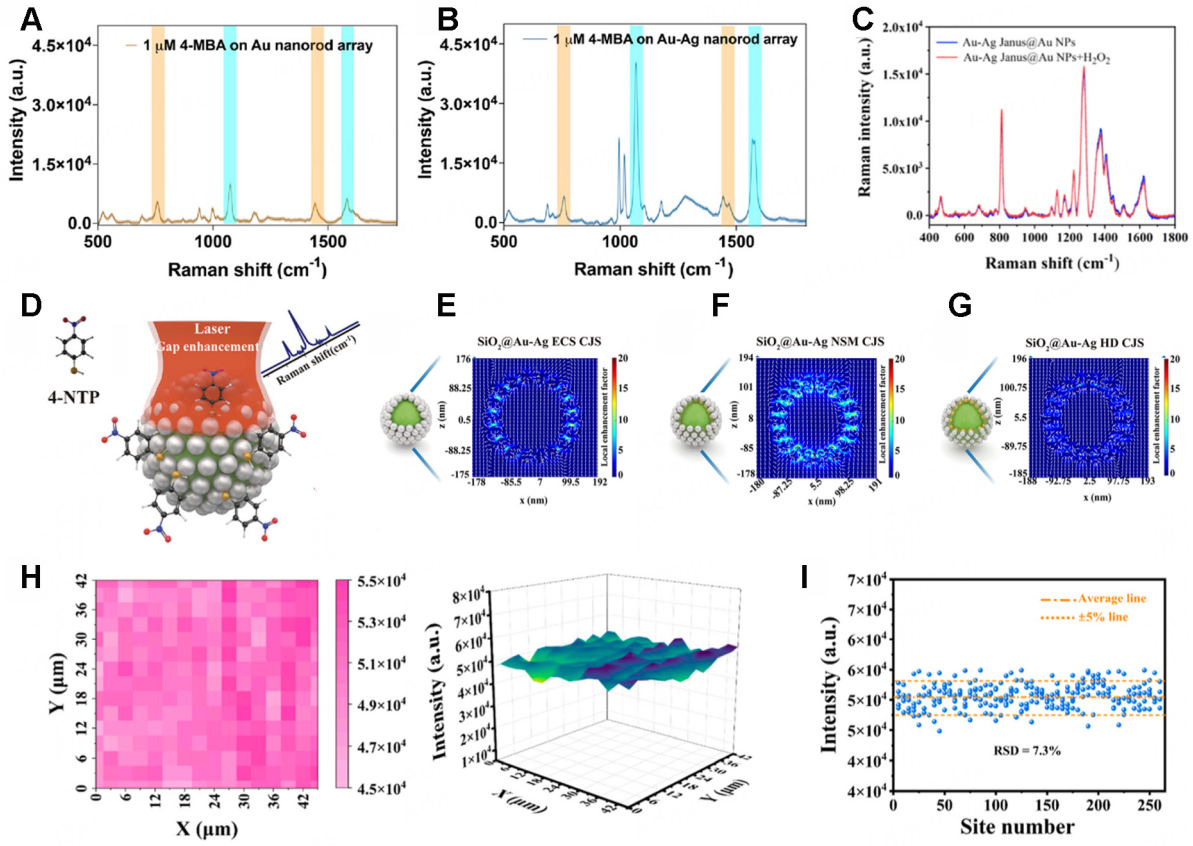

Figure 7. (A and B) The SERS spectra of 1 μM 4-MBA dropped on Au and Au-Ag nanorod arrays, with orange and cyan representing the peaks corresponding to CTAB and 4-MBA, respectively[35]. (C) SERS spectra of Au-Ag Janus@Au NPs with and without 0.1 mM H_2O_2[87]. (D) Schematic illustration of the evaluation of SERS performance using CJS components with 4-NTP as a signal molecule. (E-G) The localized electric field distribution of SiO_2@$Au_{(300)}$-Ag ECS CJS, SiO_2@$Au_{(300)}$-Ag NSM CJS, and SiO_2@$Au_{(300)}$-Ag HD CJS components, respectively, (H and I) SERS mapping at the 4-NTP peak of 1,332 cm^{-1} (42 × 45 $μm^2$) and SERS intensity distribution of 250 counts for SiO_2@$Au_{(300)}$-$Ag_{(30μL)}$ composites[110].

17.46 compared to Au-Ag Janus@Au(hollow) NPs, and by a factor of 2.27 compared to Au-Ag Janus NPs. This Raman enhancement results from the strong plasmon coupling effect between Au-Ag Janus NPs and Au dots. When hydrogen peroxide (H_2O_2) was introduced to compare the stability of Au-Ag Janus@Au NPs and Au-Ag Janus NPs, the SERS signal of the latter weakened due to the partial oxidation of the Ag islands by H_2O_2. In contrast, the SERS signal of Au-Ag Janus@Au NPs remained largely unchanged, indicating good stability [Figure 7C]. In another work, Wu *et al.* developed various plasmonic heterostructures for SERS, including Au-Ag core-shell, Janus, and core-satellite NPs. It was found that the Au-Ag core-satellite NPs with small Ag islands had the highest SERS activity[91], as the Ag islands generated more hot spots through interior gaps and high curvature. These NPs served as effective immune probes for the ultra-sensitive detection of carbohydrate antigen 19-9, achieving a wide linear range of 1.00 × 10^{-5} to 1.00 × 10^4 IU/mL and a low detection limit of 1.25 × 10^{-6} IU/mL. Hao *et al.* prepared three kinds of core-Janus satellite (CJS) structures: SiO_2@Au-Ag eccentric core-shell CJS (SiO_2@Au-Ag ECS CJS), SiO_2@Au-Ag nanosnowman-like CJS (SiO_2@Au-Ag NSM CJS), and SiO_2@Au-Ag heterogeneous dimer CJS (SiO_2@Au-Ag HD CJS)[110]. Using 4-nitrothiophenol (4-NTP) as the Raman label [Figure 7D], the SERS performance of these Janus satellite structures was evaluated, which varied in shape and density. When the number of satellites was constant, SiO_2@Au-Ag NSM CJS exhibited superior SERS activity compared to both SiO_2@Au-Ag ECS CJS and SiO_2@Au-Ag HD CJS. It is worth noting that SiO_2@Au-Ag NSM CJS has a smaller

nanogap than SiO_2@Au-Ag HD CJS, and the nanosnowman Janus structure has a smaller nanogap and a sharper neck than the eccentric core-shell Janus structure, aligning with simulation results [Figure 7E-G]. In addition, increasing satellite density significantly improved SERS activity. Among the structures tested, SiO_2@$Au_{(300)}$-Ag NSM CJS with a SiO_2-to-Au volume ratio of 1:300 achieved the highest EF of 3.04×10^8. The SERS intensity [Figure 7H] and relative standard deviation [Figure 7I] for sample SiO_2@$Au_{(300)}$-$Ag_{(30\mu L)}$ (that is, with 30 μL of $AgNO_3$ added during synthesis) demonstrated excellent uniformity and reproducibility, indicating strong potential for practical applications. It is claimed that these outstanding performances could be attributed to the well-defined and robust heterostructure which ensures a homogeneous SERS signal and reduces the effect of structural randomness on the fluctuation of the EF.

Nanogaps between the unique components of heterostructures facilitate plasmon coupling and create electromagnetic hotspots, which significantly enhance SERS activity. In most plasmonic substrates used for SERS, hotspots generally form due to nanoparticle aggregation and self-assembly, known as exterior nanogaps. In contrast, the creation of interior nanogaps within individual nanostructures results in more consistent and reliable SERS signals. In a typical study, anisotropic Au-Ag bimetallic nanostructures featuring interior hotspots could be produced by selectively overgrowing Ag NPs on the tips of Au nanostars (Au NSs)[111]. Besides, the size of these interior nanogaps could be tuned by adjusting the concentration of the Ag precursor, $AgNO_3$. As the size of the nanogaps decreased, the SERS EF increased significantly. Under 785 nm light excitation, the Au-Ag nanostructures achieved a maximum EF of 43 for the SERS signal, demonstrating better reproducibility compared to bare Au NSs. More importantly, the Au-Ag nanostructures with Ag on the tips of Au NSs showed much greater SERS enhancement than a mixture of Au NSs and similarly sized Ag NPs. This result indicated that the Raman enhancement originates from the ultrasmall nanogaps between the branches of each Au NS, which acted as intense hotspots for SERS. In another work, Wang *et al.* developed a concave Au nanocube-Ag (c-AuNC-Ag) hybrid structure that showed enhanced SERS and tunable LSPR performance[112]. Among the variants, the SERS signal of c-AuNC-Ag Janus structure was significantly enhanced under 785 nm laser excitation. In contrast, the SERS signal from the c-AuNC-Ag Janus structure was significantly greater than that of bare Ag NPs and c-AuNC seeds of similar concentration and size. Specifically, its SERS signal intensity was 17 times greater than the combined SERS intensities of Ag@5-amino-2-mercaptobenzimidazole (AMBI) NPs and c-AuNC@AMBI, and 30 times that of c-AuNC@AMBI alone. This result clearly shows that the SERS enhancement is mainly due to the strong absorption of the Janus structure near the 785 nm wavelength and the resonance of the 785 nm excited laser.

Sensing

Plasmonic metal heterostructures, due to their unique optical properties and high surface-to-volume ratio, exhibit superior performance in detecting biomolecules or chemicals and are widely used in colorimetric and spectroscopic sensing[113]. Zhao *et al.* synthesized core-shell multibranched Au NPs (MBAuNPs) coated with Ag NPs using a seed-mediated method and introduced 4-mercaptobenzonitrile (4-MBN) as Raman labels[114]. Among the tested structures, MBAuNP@4-MBN@Ag NPs exhibited the highest SERS intensity, achieving a surface EF of 1.4×10^7. Compared to the control experiment, the SERS intensity of MBAuNP@4-MBN@Ag NPs was approximately 10 times greater than that of MBAuNP. The enhanced Raman signal arose from the ultra-small gaps between the Ag shell and the MBAuNP core, which created strong hotspots for SERS. Notably, the SERS intensity of MBAuNP is over six times greater than that of spherical Au NPs (AuSNPs). This enhancement is attributed to the rough surface and branched protrusions of the nanoparticles that generate additional hotspots. Moreover, the MBAuNP@Ag nanosensor was constructed to detect endogenous H_2S in living cells, with a detection limit of approximately 0.12 nM.

Plasmonic core-satellite heterostructures are characterized by numerous hot spots resulting from plasmonic coupling between the core and the satellites, as well as among the satellites themselves, which lead to enhanced electromagnetic interactions and improved SERS effects. Theoretical predictions indicated that the electric field intensity at the interstitial sites of core-satellite assemblies was approximately 660 times greater than that on the surface of the cores[115]. Furthermore, in contrast to hot spots formed solely through particle aggregation, core-satellite structures demonstrated greater repeatability due to the strong affinity inherent in core-satellite interactions. For example, Yang *et al.* prepared an Au@Ag@SiO_2-AuNP multilayer core-shell satellite nanostructure, which was used for the detection of alpha-fetoprotein [Figure 8A][81]. It was revealed that an Ag shell with a larger thickness on the Au core and a monolayer of smaller AuNP satellites could lead to the best SERS activity. The result showed that with the increase of $AgNO_3$ volume, the Ag shell gradually thickens, and the SERS signal intensity of 4-MBA was greatly enhanced [Figure 8B]. It could be attributed to the strong electromagnetic field enhancement of Ag coating, which led to the enhancement of SERS activity. Besides, Au@Ag@SiO_2-AuNP core-shell satellite nanostructure with single-layer satellite AuNPs grown on the core of Au@Ag@SiO_2 exhibited enhanced SERS activity than its multiple-layer counterpart [Figure 8C], which was because excess satellites may cause radiation damping of incident light and reduce SERS activity. Although increased density creates more "hot spots" between the satellite and core, the SERS signals originate primarily from within the satellites rather than on their surfaces, weakening the coupling effect on Raman enhancement. As the size of the satellite AuNPs increased and approached a continuous rough shell, the SERS signal diminished due to the narrowing of gaps between coupling pairs [Figure 8D], which restricted incident light from entering the core, further reducing SERS activity. This novel structure achieved an impressive detection limit of 0.3 fg/mL and demonstrated a wide linear response range from 1 fg/mL to 1 ng/mL, showcasing its effectiveness in sensitive biomolecule detection.

Engineering the shape and architecture of the metal heterostructures could be another promising approach to enhance the sensing performances. In a typical study, various forms and compositions of metal nanomaterials were synthesized and compared for their Raman strengths[116]. At a fixed concentration of 10^{-3} M of crystal violet (CV), the Raman strength of Ag-coated Au NSs (Au@Ag CSNSs, Figure 8E) was measured at 15,182 (a.u.) at the characteristic peak of 1,171 cm^{-1}, which was approximately eight times greater than that of Au NSs. The enhanced SERS activity is attributed to the efficient plasmon coupling between the high-conductivity Ag shell and the star-shaped Au core. In contrast, spherical nanomaterials such as Ag NPs, Au NPs, and Ag-coated Au NPs exhibited lower Raman signals at 1,171 cm^{-1} compared to their star-like counterparts, including Ag NSs, Au NSs, and Au@Ag CSNSs [Figure 8F]. This enhancement arises from the branched structure, which generates more hotspots and stronger local electromagnetic fields. Besides, CV was detected using optical fiber (OF)-based sensors with Au@Ag CSNSs, achieving a minimum detection limit of approximately 5×10^{-8} M. Ding *et al.* developed an electrochemiluminescence (ECL) sensor utilizing an array structure of Au@Ag nanorods and sulfur dots[117]. It was reported that the ECL intensity of sulfur dots with ionic liquid capping (S dots (IL)) increased by 4.5 times when the Au@Ag nanorods were arranged in an array on the electrode. Notably, the ECL intensity of S dots (IL) from regularly arranged Au@Ag nanorods surpassed that from irregularly arranged nanorods. This observation suggested that the regular arrangement of Au@Ag nanorods created highly uniform and dense hot spots, enhancing the local electromagnetic field. In another work, Zhao *et al.* prepared Au nanocluster-decorated Ag@SiO_2 (Au NCs-Ag@SiO_2) nanocomposites, observing that the photocurrent reached its maximum at an optimal thickness of SiO_2 layer of 15 nm, yielding a photocurrent intensity 3.8 times greater than that of the Au NCs alone[118]. These Au NCs-Ag@SiO_2 nanocomposites were subsequently employed to construct photoelectrochemical (PEC) biosensors for detecting alkaline phosphatase activity with high sensitivity. Experimental results demonstrated that the PEC biosensor offered a low detection limit of 0.022 $U{\cdot}L^{-1}$ and a wide linear range of 0.04 to 400 $U{\cdot}L^{-1}$. Zhang *et al.* developed a Au core-4-mercaptobenzonitrile-Ag shell

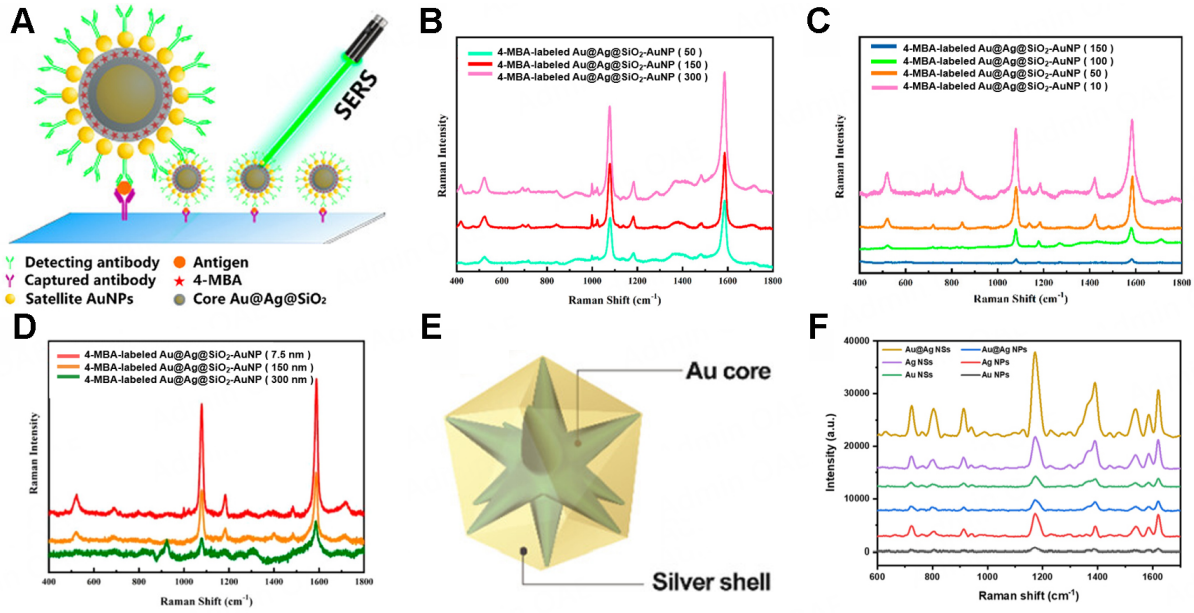

Figure 8. (A) Schematic diagram of Au@Ag @SiO_2-AuNP multilayer core-shell satellite nanostructure for the detection of alpha-fetoglobulin, (B) SERS spectra of 4-MBA-labeled Au@Ag@SiO_2-AuNP nanoassemblies with different thicknesses of silver coating, (C) SERS spectra of 4-MBA-labeled Au@Ag@SiO_2-AuNP nanoassemblies with different numbers of satellites per core and (D) SERS spectra of 4-MBA-labeled Au@Ag@SiO_2-AuNP nanoassemblies with various sizes of satellite AuNPs[81]. (E) Schematic illustration of the structure of Au@Ag CSNSs and (F) their SERS spectra using different SERS substrates[116].

nanoparticle (Au@4-MBN@Ag) as a smart SERS nanoprobe to detect endogenous H_2S in living cells based on the interaction between the Ag shell and sulfide species[119]. As the concentration of sulfide increased, more Ag_2S was generated through the reaction with the Ag shell, leading to a gradual reduction in the SERS signal intensity of Au@4-MBN@Ag. The findings indicated that the enhancing ability of Ag is significantly greater than that of Ag_2S. Notably, the formation of Ag_2S did not alter the gap between the Au core and Ag shells or the overall morphology of the nanoprobes. The result showed that the use of the Au@4-MBN@Ag nanoprobe can provide highly sensitive H_2S detection at the nM level with a detection limit of (0.14 nM). In another work, Zhu *et al.* fabricated (Au nanobipyramid)@Ag nanostructures by overgrowing Ag on monodisperse Au nanopyramids[120]. Notably, as the supply of Ag precursor increased, a structural evolution was observed, transitioning from bipyramids to rice-shaped and finally to rod structures. The Au nanobipyramid@Ag nanostructures exhibited narrower plasmon linewidths and enhanced chemical stability. This improvement was primarily attributed to the unique design of the core-shell structure, where the Au nanopyramid contributed essential plasmonic properties, and the overgrowth of Ag further enhanced these properties while providing additional chemical stability. These nanostructures were utilized to detect sulfide ions, achieving a relatively low detection limit of 0.1 × 10^{-6} M. He *et al.* prepared Au@Ag nanopencils with an Au@Ag rod and Au tip as the sensor for the detection of ClO^- and SCN^-[121]. The asymmetrical etching in different systems produced diverse variations in the LSPR peaks. In the presence of ClO^-, the Au@Ag shell remained intact while Ag was etched from the rod's tip to its end, leading to a redshift in the LSPR peak as the coupling resonance weakens. Conversely, in SCN^- and $O_2^{\bullet-}$ systems, a blue shift in the LSPR peak occurred due to a decrease in the aspect ratio as the Au@Ag rod was etched from end to tip. Experimental results indicated that the detection limits for ClO^- and SCN^- were 6.7 and 160 nM, respectively, with linear ranges of 0.05-13 and 1-600 μM, respectively.

Electrocatalysis

Plasmonic metal heterostructures have gained significant attention in the field of electrocatalysis due to their unique ability to enhance catalytic activity through synergistic effects between different metal components. It is also assumed that the superior catalytic performance of plasmonic metal heterostructures may also be related to their plasmonic effects. By combining metals with distinct electronic properties, these heterostructures can facilitate efficient charge transfer and improve the adsorption of reactants/intermediates, leading to enhanced performance in various electrochemical processes. Precise control of the configuration of metal nanostructures is crucial for enhancing electrocatalytic performance. For example, Kuhn *et al.* successfully synthesized Cu@Ag core-shell electrocatalysts by finely controlling the structures of two immiscible metals and used them for electrocatalytic carbon dioxide reduction reaction (CO_2RR)[37]. At a low initial potential of -2.25 V *vs.* reversible hydrogen electrode (RHE), it can efficiently reduce CO_2 to C_2H_4. At -2.50 V *vs.* RHE, the Faradaic efficiency (FE) for multi-carbon products (FE_{C2+}) of Cu@Ag core-shell electrocatalysts with an optimal Ag shell thickness of 0.15 nm reached 43% [Figure 9A], while the FE_{C2+} of Cu catalyst was only about one-third of that of the Cu@Ag core-shell catalyst [Figure 9B]. This phenomenon can be attributed to the increased concentration of surface-bound CO^* species on the Cu@Ag catalyst, which enhances the C-C coupling process for the production of multi-carbon products. In the tandem catalytic process of the Cu@Ag core-shell structure, CO_2 was first adsorbed, activated, and reduced to CO on the Ag shell, which was then further converted into C_{2+} products via reactions on the Cu core, realizing a two-step CO_2RR process [Figure 9C]. Thus, the thickness of the Ag shell significantly influences the selectivity and activity during CO_2RR. Zhang *et al.* synthesized Cu@Ag core-shell nanoparticles with different sizes of 10.7, 11.2, 11.8, and 12.2 nm (denoted as Cu@Ag-1, Cu@Ag-2, Cu@Ag-3, and Cu@Ag-4, respectively)[78]. It was reported that the Cu@Ag-2 NP showed high FEs of 67.6% and 32.2% towards C_2 products and ethylene, respectively, both higher than that of the other three Cu@Ag NPs with different thicknesses of the Ag shell [Figure 9D and E]. Besides, the production of H_2 was effectively inhibited on Cu@Ag heterostructures as compared to Cu NPs and the mixture of Cu and Ag NPs, suggesting that the core-shell heterostructure is beneficial for CO_2RR. It is claimed that the appropriate synergistic interaction between the Cu core and Ag shell enhanced the binding strength of CO on the Cu/Ag interface, accelerated charge transfer, and increased the electrochemical surface area, which led to improved catalytic performance.

Optimizing the local confinement effect within the metal heterostructures is another effective way to increase the concentration of local CO intermediates and thus improve the selectivity of CO_2RR toward C_{2+} products by promoting the C-C coupling reaction. For example, Zhong *et al.* designed Ag@Cu catalysts with porous Cu shells of different pore sizes and investigated the confinement effect of different Cu shells on the selectivity of CO_2RR toward C_{2+} products[77]. Under all constant current density, the Ag@Cu core-shell catalyst with a pore size of 4.9 nm, named Ag@Cu-p4.9 nm, exhibited superior catalytic activity and selectivity compared to the other core-shell catalysts with different pore sizes. Specifically, Ag@Cu-p4.9 nm achieved the highest FE of 73.7% for C_{2+} products at the current density of 300 mA cm^{-2}, and a selectivity ratio of C_{2+}/C_1 products of 5.1 at the current density of 400 mA cm^{-2} [Figure 9F]. As a comparison, CO is the dominant product during CO_2RR over monometallic Ag catalysts at different current densities. It is reported that the Ag@Cu-p4.9 with suitable pore size could exhibit the highest local CO concentration on the surface of the Cu pore as indicated by the highest *CO coverage *in situ* attenuated total reflection surface-enhanced infrared absorption spectroscopy results, which further promotes the subsequent C-C coupling and leads to the highest C_{2+} selectivity.

The spatial distribution of different metal components within the metal heterostructures is a key factor that influences the reaction process during CO_2RR for the production of different products, especially multi-carbon products. In a typical work, Huang *et al.* synthesized Janus Ag-Cu NDs with a tunable size of the Cu

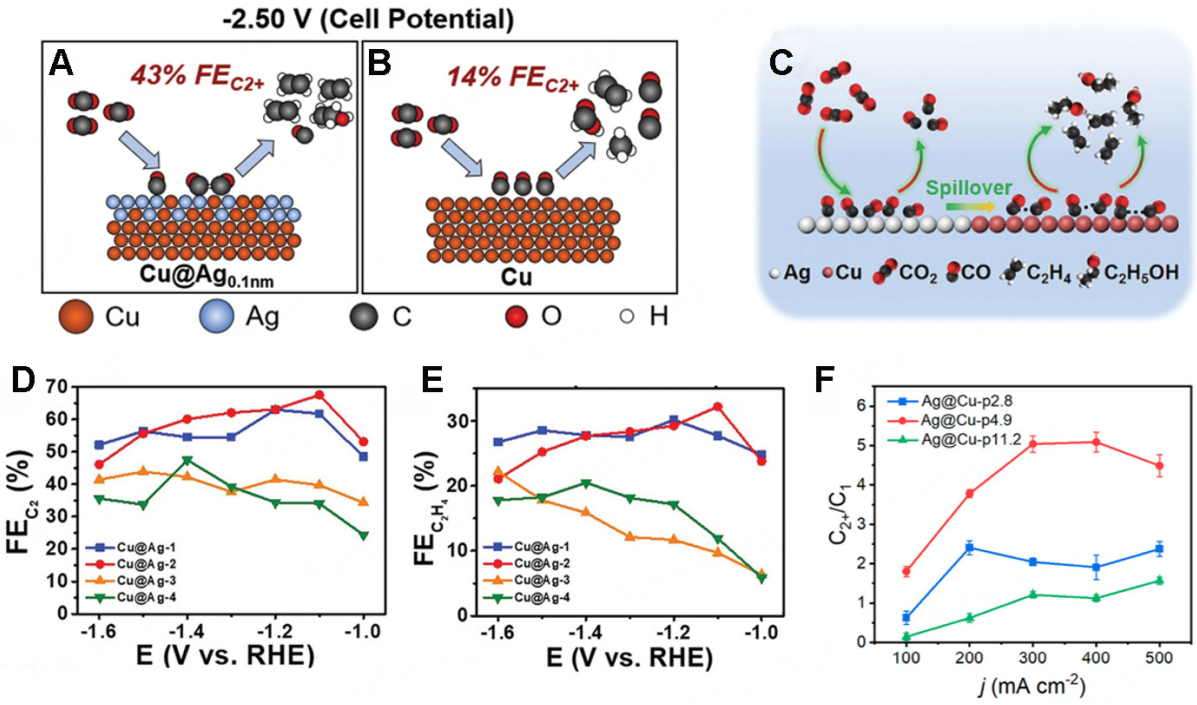

Figure 9. (A) Schematic illustration of the FE of C_{2+} products for CO_2RR by Cu@Ag core-shell catalyst and (B) Schematic illustration of the FE of C_{2+} products for CO_2RR at low potentials by Cu catalyst[37]. (C) Schematic illustration of the catalytic mechanism of Cu@Ag heterostructure , (D) FE for C_2 products and (E) FE for C_2H_4 of Cu@Ag core-shell catalysts[78]. (F) Ratio between FE for C_{2+}/C_1 products of Ag@Cu catalysts with different pore sizes[77].

domain as an electrocatalyst for tandem CO_2RR[94]. Among various catalysts, Ag_1-$Cu_{1.1}$ NDs with Ag/Cu mass ratio of 1:1.1 showed the highest FE of approximately 40% towards the production of C_2H_4 at -1.1 V *vs.* RHE, which surpassed other Ag-Cu NDs with different mass ratios and the mixture of Ag and Cu nanoparticles, indicating the importance of the spatial distribution. It is also worth noting that Cu nanoparticles with similar size and shape only exhibited a FE of approximately 12% for C_2H_4 [Figure 10A], and its current density is only half that of Ag_1-$Cu_{1.1}$ NDs [Figure 10B], suggesting the important role of metal heterostructures for the production of multi-carbon products. It is claimed that the tandem catalysis and the unique electronic structure of the Ag-Cu ND are key factors contributing to its improved C_2H_4 selectivity and enhanced activity. In another work, Zhang *et al.* addressed the issue of the lack of tunability in Cu-based heterostructures and systematically studied the effect of Cu spatial distribution in Au-Cu HSs on the selectivity of CO_2RR[93]. As the contact area between Au and Cu increases, three kinds of Janus nanostructures (Au-Cu_I, Au-Cu_{II}, Au-Cu_{III}) and core-shell nanostructures (Au-Cu_{IV}) were formed. It is found that the Au-Cu_{III} catalyst showed a maximum FE towards C_{2+} products of 80% with a high partial current density of 466.1 mA cm^{-2} [Figure 10C], while the monometallic Au catalyst only produces CO and H_2 during CO_2RR, indicating that the adsorbed *CO intermediates can be further converted to multi-carbon products and the production of H_2 can be inhibited on Au-Cu HSs. More interestingly, the primary product during CO_2RR is switchable by tuning the interface of Au-Cu HSs. As shown in Figure 10D, the primary product could be tuned from CH_3OH (FE of 72.1% in liquid products on Au-Cu_I) to C_2H_5OH (FE of 78.1% in liquid products on Au-Cu_{II}) and C_2H_4 (FE of 63% in gas products on Au-Cu_{III}). Then, operando surface-enhanced Raman spectroscopy and density functional theory (DFT) calculations showed that the reaction pathway during CO_2RR can be modulated on different Au-Cu HSs which facilitate the production of various products. Ma *et al.* studied the tandem CO_2RR process over three types of Ag-Cu Janus nanostructures with exposed {100} facets (Ag-Cu JNS-100) and different atomic ratios between Ag and

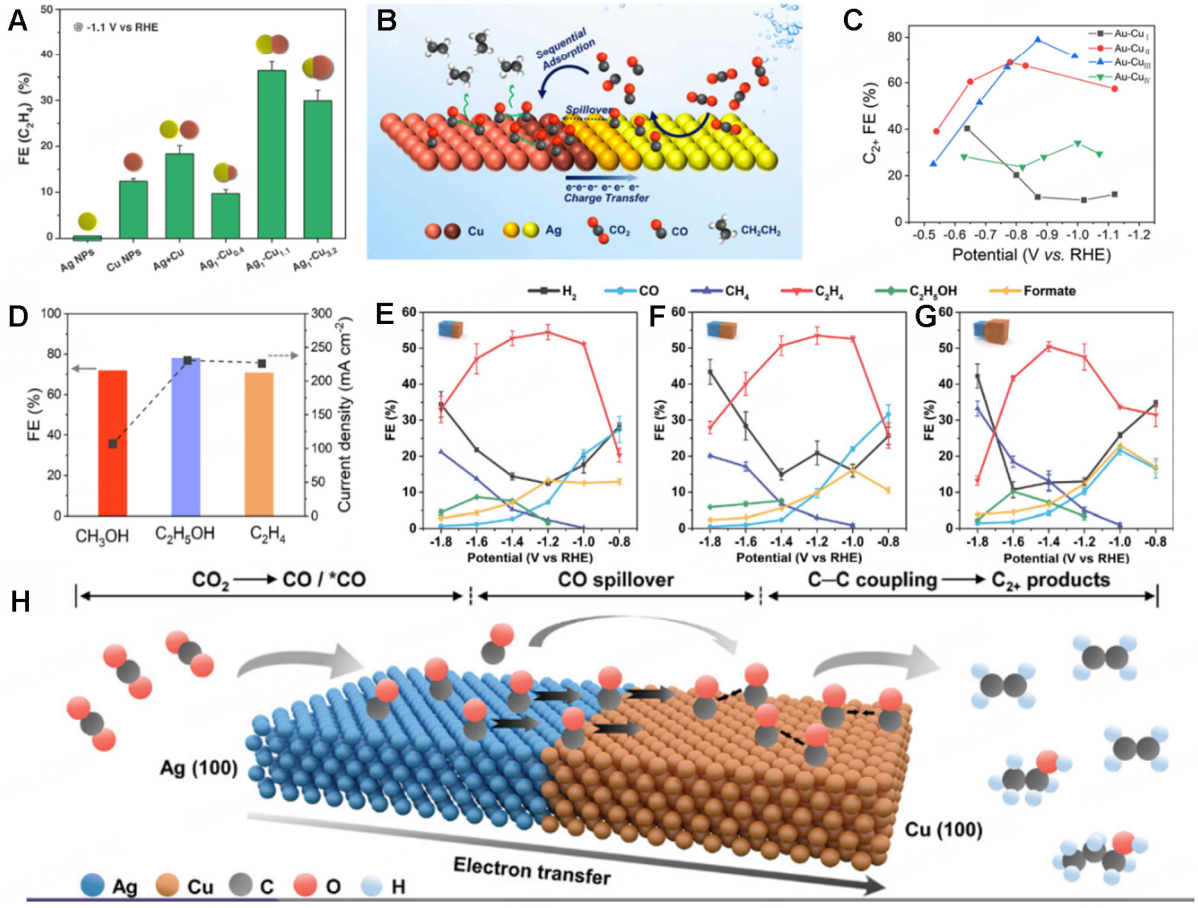

Figure 10. (A) FE of C_2H_4 obtained at -1.1 V *vs.* RHE on various Ag/Cu nanocrystals and (B) Schematic illustration of the mechanism during CO_2RR in Ag-Cu NDs[94]. (C) FEs for C_{2+} products of Au-Cu catalysts in different potentials and (D) Maximum FE and corresponding partial current densities of CH_3OH, C_2H_5OH, and C_2H_4 in Au-Cu_I, Au-Cu_{II}, and Au-Cu_{III}[93]. (E-G) Electrocatalytic performance of Ag-Cu JNS-100: Ag_{65}-Cu_{35} JNS-100 (E), Ag_{50}-Cu_{50} JNS-100 (F), and Ag_{25}-Cu_{75} JNS-100 (G) and (H) CO_2RR mechanism for Ag-Cu JNS-100[95].

Cu[95]. It is found that all three Ag-Cu Janus heterostructures showed high FEs of over 50% towards the production of C_{2+} products in their optimal potentials [Figure 10E-G], which is much superior to those of Cu (52%) and the mixture of Ag and Cu (22%), indicating the importance of constructing metal heterostructures for enhanced CO_2RR performances. Among them, Ag_{65}-Cu_{35} JNS-100 with an Ag/Cu ratio of 65/35 exhibited a maximum FE of 54% and 72% for the production of C_2H_4 and C_{2+} products. The reaction mechanism during the CO_2RR process is illustrated in Figure 10H. First, the Ag domain of Jansu Ag-Cu would convert CO_2 into CO or *CO intermediates, which then spill over to the nearby Cu (100) domain and were further reduced to C_2H_4. The theoretical calculation result suggested that the excellent CO_2RR performance of Ag_{65}-Cu_{35} JNS-100 could be attributed to the modified electronic structure and the promoted CO spillover effect, which reduces the energy barrier for the production of C_{2+} products.

Plasmonic metal heterostructures could show great promise in plasmon-enhanced electrocatalysis due to the unique optical properties of plasmonic metals. Under light irradiation, plasmonic materials could generate localized thermal effects and produce energetic hot carriers (hot electrons and holes) during plasmon decay[122,123], which could enhance electrocatalytic performance. For example, the high energy of hot holes contributes significantly to oxidation reactions by directly interacting with adsorbed molecules and

facilitating bond cleavage if they could be transferred to a catalyst[124,125]. For example, Corson *et al.* reported the plasmon-enhanced CO_2RR performance of Cu-Ag heterostructure[126]. Specifically, the production of CO could be enhanced while the hydrogen evolution was inhibited under light irradiation at low overpotentials at -0.6 and -0.7 V *vs.* RHE. It was claimed that the enhanced CO production after light irradiation was ascribed to the hot electrons transferred to the metal-CO complex, accelerating CO desorption, while the increased local electric field enhanced the bonding of HCO_3^- on the surface of the catalyst, thus lowering the local pH and suppressing H_2 evolution. At high overpotentials of -0.9 and -1.0 V *vs.* RHE, the Cu-Ag heterostructures could show higher FEs towards the production of ethylene, methane, formate, and allyl alcohols with the light irradiation, showing a plasmon-enhanced electrocatalytic performance. It is also worth noting that the effect of local heating under light showed no contribution to the enhanced FE after conducting temperature-dependent experiments.

CONCLUSION AND PERSPECTIVE

In conclusion, this review summarizes the latest advances in the synthesis of plasmonic metal heterostructures composed of plasmonic metals (Au, Ag, Cu), along with their applications in SERS, sensing, and electrocatalysis. The synergistic effects and interactions between different components in plasmonic metal heterostructures can enhance the physicochemical properties of the materials, thereby significantly improving their performance in various applications. Despite the considerable progress made over the past decade, key challenges remain in the synthesis and application of plasmonic metal-based heterostructures, thus simultaneously generating many exciting future research directions.

First, the seed-mediated growth method is widely used for synthesizing plasmonic metal heterostructures. However, even minor changes in synthesis conditions (such as temperature, pH value, surfactant, and precursor concentration) during the growth can significantly affect the size and shape of the resultant nanocrystals, making large-scale production challenging. Meanwhile, many existing methods are based on selectively depositing other materials on plasmonic metal nanocrystals to synthesize plasmonic metal heterostructures, which often involve multiple steps. Therefore, it is urgent to develop simple and reliable synthetic methods for large-scale and robust synthesis of more kinds of plasmonic metal heterostructures. Secondly, the technology for precise morphological control of plasmonic metal heterostructures has not yet been fully developed. Additionally, the formation mechanism and structure-performance relationships of plasmonic metal heterostructures have not yet been clarified. A deep understanding of the structural correlations and synergistic effects between different components in metal heterostructures is needed, which can guide us to comprehensively control the architecture of heterostructures and enhance their functionality and diversity for various applications. Also, a systematic model for the formation mechanism can be established by recording the experimental process, especially with the aid of some in situ observation techniques. Furthermore, with the help of computational methods, emerging theoretical simulations, and machine learning technologies, it is possible to propose and predict suitable metal heterostructures tailored for specific applications, providing valuable guidance for the synthesis of target materials in experiments. Thirdly, designing plasmonic metal heterostructures with a uniform distribution of hotspots and repeatability is crucial for enhancing performance in SERS and sensing. However, current synthesis methods have difficulty in achieving consistent and uniform hot spots in mass production. It is imperative to systematically refine the synthetic process and develop new precise synthetic approaches. For example, novel technologies such as layer-by-layer assembly or controlled deposition methods can be developed to allow for precise control over the morphology and dimensions of the heterostructures. To further ensure the precise synthesis of plasmonic metal heterostructures with desired properties, one may also employ machine learning to illustrate and even predict the effects of different synthetic parameters on their hotspot distribution. Fourthly, although plasmonic metal heterostructures have been demonstrated as excellent

catalysts for diverse reactions, the role of the plasmonic effect produced by plasmonic metal components in enhancing their catalytic performance has not been clearly identified, which hinders the further development of high-performance catalysts with promising applications. Fifthly, combining plasmonic metal heterostructures with other functional components, such as semiconductors, and 2D materials is a promising approach to obtain novel functionalities and enhance their optical, electronic, and catalytic performances. Sixthly, compared to traditional plasmonic metals such as Au and Ag with high cost, Al-based nanomaterials show cost-effectiveness, high abundance, and tunable plasmonic properties, however, whose development is still limited due to the lack of robust synthetic strategies. Advances in the controlled synthesis of Al-based nanomaterials could pave new avenues for practical applications of plasmonic metal nanomaterials. Last but not least, the potential applications of plasma metal heterostructures still need to be developed besides SERS, sensing, and electrocatalysis. Depending on different requirements for versatile applications, various types of plasmonic metal heterostructures with distinct architectures and compositions could be rationally designed and prepared to broaden their application potential.

DECLARATIONS

Author's contributions

Conceptualization, investigation, and writing-original draft: Wang, H.; Huang, B.
Writing-review & editing: Chen, G. J.; Huang, B.; Xue, C.; Kuang, J.
Writing-review & editing, supervision, and funding acquisition: Cong, L.; Shum, P. P.; Ge, Y.

Availability of data and materials

Not applicable.

Financial support and sponsorship

This work was supported by the National Natural Science Foundation of China (52471219), Start-Up Grant from University of Science and Technology Beijing (00007838), National Natural Science Foundation of China (62220106006, 62361136584), Shenzhen Science and Technology Program (SGDX20211123114001001, JSGGKQTD20221101115656030), Guangdong Basic and Applied Basic Research Foundation (2021B1515120013), and High Level of Special Funds (G030230001, G03034K004) from Southern University of Science and Technology.

Conflicts of interest

All authors declared that there are no conflicts of interest.

Ethical approval and consent to participate

Not applicable.

Consent for publication

Not applicable.

REFERENCES

1. Kang, G.; Hu, S.; Guo, C.; Arul, R.; Sibug-Torres, S. M.; Baumberg, J. J. Design rules for catalysis in single-particle plasmonic nanogap reactors with precisely aligned molecular monolayers. *Nat. Commun.* **2024**, *15*, 9220. DOI PubMed PMC
2. Zhang, X.; Gao, D.; Zhu, B.; Cheng, B.; Yu, J.; Yu, H. Enhancing photocatalytic H_2O_2 production with Au co-catalysts through electronic structure modification. *Nat. Commun.* **2024**, *15*, 3212. DOI PubMed PMC
3. Park, S. H.; Kim, S.; Park, J. W.; Kim, S.; Cha, W.; Lee, J. In-situ and wavelength-dependent photocatalytic strain evolution of a

single Au nanoparticle on a TiO_2 film. *Nat. Commun.* **2024**, *15*, 5416. DOI PubMed PMC

4. Kang, Y.; João, S. M.; Lin, R.; et al. Effect of crystal facets in plasmonic catalysis. *Nat. Commun.* **2024**, *15*, 3923. DOI PubMed PMC
5. Wu, H.; Yu, H.; Chow, Y. L.; Webley, P. A.; Zhang, J. Toward durable CO_2 electroreduction with Cu-based catalysts via understanding their deactivation modes. *Adv. Mater.* **2024**, *36*, e2403217. DOI
6. Liu, S.; Tao, H.; Zeng, L.; et al. Shape-dependent electrocatalytic reduction of CO_2 to CO on triangular silver nanoplates. *J. Am. Chem. Soc.* **2017**, *139*, 2160-3. DOI
7. Li, H.; Du, H.; Luo, H.; Wang, H.; Zhu, W.; Zhou, Y. Recent developments in metal nanocluster-based catalysts for improving photocatalytic CO_2 reduction performance. *Microstructures* **2023**, *3*, 2023024. DOI
8. Qu, J.; Cao, X.; Gao, L.; et al. Electrochemical carbon dioxide reduction to ethylene: from mechanistic understanding to catalyst surface engineering. *Nanomicro. Lett.* **2023**, *15*, 178. DOI PubMed PMC
9. Wang, D.; Mao, J.; Zhang, C.; et al. Modulating microenvironments to enhance CO_2 electroreduction performance. *eScience* **2023**, *3*, 100119. DOI
10. Niu, Z. Z.; Chi, L. P.; Wu, Z. Z.; Yang, P. P.; Fan, M. H.; Gao, M. R. CO_2-assisted formation of grain boundaries for efficient CO-CO coupling on a derived Cu catalyst. *Natl. Sci. Open.* **2023**, *2*, 20220044. DOI
11. Yuan, X.; Shen, D.; Zhang, Q.; Zou, H.; Liu, Z.; Peng, F. Z-scheme $Bi_2WO_6/CuBi_2O_4$ heterojunction mediated by interfacial electric field for efficient visible-light photocatalytic degradation of tetracycline. *Chem. Eng. J.* **2019**, *369*, 292-301. DOI
12. Li, J.; Lou, Z.; Li, B. Nanostructured materials with localized surface plasmon resonance for photocatalysis. *Chin. Chem. Lett.* **2022**, *33*, 1154-68. DOI
13. Wang, T.; Wang, H.; Lin, J.; et al. Plasmonic photocatalysis: mechanism, applications and perspectives. *Chin. J. Struct. Chem.* **2023**, *42*, 100066. DOI
14. Lin, W.; Ghulam, N. A.; Palma, M.; Di, T. D. Copper nanowires for electrochemical CO_2 reduction reaction. *ACS. Appl. Nano. Mater.* **2024**, *7*, 27883-98. DOI
15. Jang, Y. H.; Jang, Y. J.; Kim, S.; Quan, L. N.; Chung, K.; Kim, D. H. Plasmonic solar cells: from rational design to mechanism overview. *Chem. Rev.* **2016**, *116*, 14982-5034. DOI
16. Cheng, P.; Ziegler, M.; Ripka, V.; et al. Black silver: three-dimensional Ag hybrid plasmonic nanostructures with strong photon coupling for scalable photothermoelectric power generation. *ACS. Appl. Mater. Interfaces.* **2022**, *14*, 16894-900. DOI
17. Zhang, S.; Huang, F.; Guo, X.; et al. Boosting the efficiency of dye-sensitized solar cells by a multifunctional composite photoanode to 14.13. *Angew. Chem. Int. Ed.* **2023**, *62*, e202302753. DOI
18. Phengdaam, A.; Nootchanat, S.; Ishikawa, R.; et al. Improvement of organic solar cell performance by multiple plasmonic excitations using mixed-silver nanoprisms. *J. Sci. Adv. Mater. Dev.* **2021**, *6*, 264-70. DOI
19. Lee, S.; Dang, H.; Moon, J. I.; et al. SERS-based microdevices for use as in vitro diagnostic biosensors. *Chem. Soc. Rev.* **2024**, *53*, 5394-427. DOI
20. Chang, K.; Zhao, Y.; Wang, M.; et al. Advances in metal-organic framework-plasmonic metal composites based SERS platforms: engineering strategies in chemical sensing, practical applications and future perspectives in food safety. *Chem. Eng. J.* **2023**, *459*, 141539. DOI
21. Li, Z.; Zhai, L.; Zhang, Q.; et al. 1T'-transition metal dichalcogenide monolayers stabilized on 4H-Au nanowires for ultrasensitive SERS detection. *Nat. Mater.* **2024**, *23*, 1355-62. DOI
22. Liu, Y.; Ma, H.; Han, X. X.; Zhao, B. Metal-semiconductor heterostructures for surface-enhanced Raman scattering: synergistic contribution of plasmons and charge transfer. *Mater. Horiz.* **2021**, *8*, 370-82. DOI PubMed
23. Belushkin, A.; Yesilkoy, F.; Altug, H. Nanoparticle-enhanced plasmonic biosensor for digital biomarker detection in a microarray. *ACS. Nano.* **2018**, *12*, 4453-61. DOI
24. Yang, W.; Lim, D. K. Recent advances in the synthesis of intra-nanogap Au plasmonic nanostructures for bioanalytical applications. *Adv. Mater.* **2020**, *32*, e2002219. DOI PubMed
25. Chen, Y.; Bai, Y.; Wang, X.; Zhang, H.; Zheng, H.; Gu, N. Plasmonic/magnetic nanoarchitectures: from controllable design to biosensing and bioelectronic interfaces. *Biosens. Bioelectron.* **2023**, *219*, 114744. DOI
26. Fan, Z.; Bosman, M.; Huang, Z.; et al. Heterophase fcc-2H-fcc gold nanorods. *Nat. Commun.* **2020**, *11*, 3293. DOI PubMed PMC
27. Linic, S.; Aslam, U.; Boerigter, C.; Morabito, M. Photochemical transformations on plasmonic metal nanoparticles. *Nat. Mater.* **2015**, *14*, 567-76. DOI PubMed
28. Ha, M.; Kim, J. H.; You, M.; Li, Q.; Fan, C.; Nam, J. M. Multicomponent plasmonic nanoparticles: from heterostructured nanoparticles to colloidal composite nanostructures. *Chem. Rev.* **2019**, *119*, 12208-78. DOI
29. Cha, S. K.; Mun, J. H.; Chang, T.; et al. Au-Ag core-shell nanoparticle array by block copolymer lithography for synergistic broadband plasmonic properties. *ACS. Nano.* **2015**, *9*, 5536-43. DOI
30. Wang, X.; Ge, Y.; Sun, M.; et al. Facet-controlled synthesis of unconventional-phase metal alloys for highly efficient hydrogen oxidation. *J. Am. Chem. Soc.* **2024**, *146*, 24141-9. DOI
31. Ge, Y.; Wang, X.; Chen, B.; et al. Preparation of fcc-2H-fcc Heterophase Pd@Ir nanostructures for high-performance electrochemical hydrogen evolution. *Adv. Mater.* **2022**, *34*, e2107399. DOI
32. Ge, Y.; Huang, Z.; Ling, C.; et al. Phase-selective epitaxial growth of heterophase nanostructures on unconventional 2H-Pd nanoparticles. *J. Am. Chem. Soc.* **2020**, *142*, 18971-80. DOI

33. Zhu, J.; Jia, T. T.; Li, J. J.; Li, X.; Zhao, J. W. Plasmonic spectral determination of Hg(II) based on surface etching of Au-Ag core-shell triangular nanoplates: From spectrum peak to dip. *Spectrochim. Acta. A. Mol. Biomol. Spectrosc.* **2019**, *207*, 337-47. DOI
34. Yang, X. Q.; Lu, Y.; Liu, Y.; Wang, J.; Shao, L.; Wang, J. F. Heterostructures built through site-selective deposition on anisotropic plasmonic metal nanocrystals and their applications. *Small. Struct.* **2021**, *2*, 2100101. DOI
35. Tanwar, S.; Anantha, P.; Wu, L.; Barman, I. Self-assembled bimetallic Au-Ag nanorod vertical array for single molecule plasmonic sensing. *ACS. Appl. Nano. Mater.* **2024**, *7*, 1636-45. DOI PubMed PMC
36. Wu, F.; Xia, S.; Wei, J.; Gao, W.; Li, F.; Niu, W. Metallic heterostructures for plasmon-enhanced electrocatalysis. *Chemphyschem* **2023**, *24*, e202200881. DOI
37. Kuhn, A. N.; Zhao, H.; Nwabara, U. O.; et al. Engineering silver-enriched copper core-shell electrocatalysts to enhance the production of ethylene and C_{2+} chemicals from carbon dioxide at low cell potentials. *Adv. Funct. Mater.* **2021**, *31*, 2101668. DOI
38. Kim, S.; Kim, J. M.; Park, J. E.; Nam, J. M. Nonnoble-metal-based plasmonic nanomaterials: recent advances and future perspectives. *Adv. Mater.* **2018**, *30*, e1704528. DOI
39. Bodelón, G.; Costas, C.; Pérez-Juste, J.; Pastoriza-Santos, I.; Liz-Marzán, L. M. Gold nanoparticles for regulation of cell function and behavior. *Nano. Today.* **2017**, *13*, 40-60. DOI
40. Ross, M. B.; Schatz, G. C. Aluminum and indium plasmonic nanoantennas in the ultraviolet. *J. Phys. Chem. C.* **2014**, *118*, 12506-14. DOI
41. Kim, T. I.; Park, I. J.; Choi, S. Y. Synthesis of ultrathin metal nanowires with chemically exfoliated tungsten disulfide nanosheets. *Nano. Lett.* **2020**, *20*, 3740-6. DOI PubMed
42. Chen, J.; Feng, J.; Yang, F.; Aleisa, R.; Zhang, Q.; Yin, Y. Space-confined seeded growth of Cu nanorods with strong surface plasmon resonance for photothermal actuation. *Angew. Chem. Int. Ed.* **2019**, *58*, 9275-81. DOI
43. Lu, S.; Yu, H.; Gottheim, S.; et al. Polymer-directed growth of plasmonic aluminum nanocrystals. *J. Am. Chem. Soc.* **2018**, *140*, 15412-8. DOI
44. Robatjazi, H.; Lou, M.; Clark, B. D.; et al. Site-selective nanoreactor deposition on photocatalytic Al nanocubes. *Nano. Lett.* **2020**, *20*, 4550-7. DOI
45. Shi, Y.; Lyu, Z.; Zhao, M.; Chen, R.; Nguyen, Q. N.; Xia, Y. Noble-metal nanocrystals with controlled shapes for catalytic and electrocatalytic applications. *Chem. Rev.* **2021**, *121*, 649-735. DOI
46. Huo, D.; Kim, M. J.; Lyu, Z.; Shi, Y.; Wiley, B. J.; Xia, Y. One-dimensional metal nanostructures: from colloidal syntheses to applications. *Chem. Rev.* **2019**, *119*, 8972-9073. DOI PubMed
47. Zhang, L.; Doyle-Davis, K.; Sun, X. Pt-based electrocatalysts with high atom utilization efficiency: from nanostructures to single atoms. *Energy. Environ. Sci.* **2019**, *12*, 492-517. DOI
48. McGrath, A. J.; Chien, Y. H.; Cheong, S.; et al. Gold over branched palladium nanostructures for photothermal cancer therapy. *ACS. Nano.* **2015**, *9*, 12283-91. DOI
49. Chen, J.; Zhou, J.; Peng, Y.; et al. Highly-adaptable optothermal nanotweezers for trapping, sorting, and assembling across diverse nanoparticles. *Adv. Mater.* **2024**, *36*, e2309143. DOI
50. Chen, J.; Chen, Z.; Meng, C.; et al. CRISPR-powered optothermal nanotweezers: diverse bio-nanoparticle manipulation and single nucleotide identification. *Light. Sci. Appl.* **2023**, *12*, 273. DOI PubMed PMC
51. Feng, Q.; Zhao, X.; Guo, Y.; Liu, M.; Wang, P. Stochastic DNA walker for electrochemical biosensing sensitized with gold nanocages@graphene nanoribbons. *Biosens. Bioelectron.* **2018**, *108*, 97-102. DOI
52. Yin, B. S.; Hu, J. Q.; Ding, S. Y.; et al. Identifying mass transfer influences on Au nanoparticles growth process by centrifugation. *Chem. Commun.* **2012**, *48*, 7353-5. DOI
53. Boas, D.; Remennik, S.; Reches, M. Peptide-capped Au and Ag nanoparticles: detection of heavy metals and photochemical core/shell formation. *J. Colloid. Interface. Sci.* **2023**, *631*, 66-76. DOI PubMed
54. Li, Z. Y.; Young, N. P.; Di, V. M.; et al. Three-dimensional atomic-scale structure of size-selected gold nanoclusters. *Nature* **2008**, *451*, 46-8. DOI
55. Qin, Y.; Wu, Y.; Wang, B.; Wang, J.; Yao, W. Facile synthesis of Ag@Au core-satellite nanowires for highly sensitive SERS detection for tropane alkaloids. *J. Alloys. Compd.* **2021**, *884*, 161053. DOI
56. Hussain, S.; Pal, A. Incorporation of nanocrystalline silver on carbon nanotubes by electrodeposition technique. *Mater. Lett.* **2008**, *62*, 1874-7. DOI
57. Khodashenas, B.; Ghorbani, H. R. Synthesis of silver nanoparticles with different shapes. *Arabian. J. Chem.* **2019**, *12*, 1823-38. DOI
58. García de Abajo, F. J. *Colloquium*: light scattering by particle and hole arrays. *Rev. Mod. Phys.* **2007**, *79*, 1267-90. DOI
59. El-Nour KM, Eftaiha A, Al-Warthan A, Ammar RA. Synthesis and applications of silver nanoparticles. *Arabian. J. Chem.* **2010**, *3*, 135-40. DOI
60. Zhao, Y.; Liu, L.; Kuang, H.; Wang, L.; Xu, C. SERS-active Ag@Au core-shell NP assemblies for DNA detection. *RSC. Adv.* **2014**, *4*, 56052-6. DOI
61. Zhang, P.; Sui, Y.; Wang, C.; et al. A one-step green route to synthesize copper nanocrystals and their applications in catalysis and surface enhanced Raman scattering. *Nanoscale* **2014**, *6*, 5343-50. DOI
62. Hsia, C.; Chang, C.; Huang, M. H. Unusually large lattice mismatch-induced optical behaviors of Au@Cu-Cu_2O core-shell nanocrystals with noncentrally located cores. *Part. Part. Syst. Charact.* **2018**, *35*, 1800112. DOI
63. Roberts, F. S.; Kuhl, K. P.; Nilsson, A. Electroreduction of carbon monoxide over a copper nanocube catalyst: surface structure and

pH dependence on selectivity. *ChemCatChem* **2016**, *8*, 1119-24. DOI

64. Jeon, H. S.; Kunze, S.; Scholten, F.; Roldan, C. B. Prism-shaped Cu nanocatalysts for electrochemical CO_2 reduction to ethylene. *ACS. Catal.* **2018**, *8*, 531-5. DOI
65. Lee, J. W.; Han, J.; Lee, D. S.; et al. 2D single-crystalline copper nanoplates as a conductive filler for electronic ink applications. *Small* **2018**, *14*, 1703312. DOI
66. Hoang, T. T. H.; Ma, S.; Gold, J. I.; Kenis, P. J. A.; Gewirth, A. A. Nanoporous copper films by additive-controlled electrodeposition: CO_2 reduction catalysis. *ACS. Catal.* **2017**, *7*, 3313-21. DOI
67. Wang, Y.; Shen, H.; Livi, K. J. T.; et al. Copper nanocubes for CO_2 reduction in gas diffusion electrodes. *Nano. Lett.* **2019**, *19*, 8461-8. DOI
68. Nitopi, S.; Bertheussen, E.; Scott, S. B.; et al. Progress and perspectives of electrochemical CO_2 reduction on copper in aqueous electrolyte. *Chem. Rev.* **2019**, *119*, 7610-72. DOI
69. Lei, Q.; Zhu, H.; Song, K.; et al. Investigating the origin of enhanced C_{2+} selectivity in oxide-/hydroxide-derived copper electrodes during CO_2 electroreduction. *J. Am. Chem. Soc.* **2020**, *142*, 4213-22. DOI
70. Ma, Z.; Tsounis, C.; Kumar, P. V.; et al. Enhanced electrochemical CO_2 reduction of Cu@Cu_xO nanoparticles decorated on 3D vertical graphene with intrinsic sp^3-type defect. *Adv. Funct. Mater.* **2020**, *30*, 1910118. DOI
71. Hang, Y.; Wang, A.; Wu, N. Plasmonic silver and gold nanoparticles: shape- and structure-modulated plasmonic functionality for point-of-caring sensing, bio-imaging and medical therapy. *Chem. Soc. Rev.* **2024**, *53*, 2932-71. DOI PubMed PMC
72. Huang, Z.; Meng, G.; Hu, X.; et al. Plasmon-tunable Au@Ag core-shell spiky nanoparticles for surface-enhanced Raman scattering. *Nano. Res.* **2019**, *12*, 449-55. DOI
73. Qi, Y.; Xing, T.; Zhao, J.; et al. Tuning the surface enhanced Raman scattering performance of anisotropic Au core-Ag shell hetero-nanostructure: the effect of core geometry. *J. Alloys. Compd.* **2019**, *776*, 934-47. DOI
74. Hsia, C.; Madasu, M.; Huang, M. H. Aqueous phase synthesis of Au-Cu core-shell nanocubes and octahedra with tunable sizes and noncentrally located cores. *Chem. Mater.* **2016**, *28*, 3073-9. DOI
75. Lyu, Z.; Xie, M.; Aldama, E.; et al. Au@Cu core-shell nanocubes with controllable sizes in the range of 20-30 nm for applications in catalysis and plasmonics. *ACS. Appl. Nano. Mater.* **2019**, *2*, 1533-40. DOI
76. Wang, Y.; Kong, J.; Xue, R.; et al. Highly stable, stretchable, and transparent electrodes based on dual-headed Ag@Au core-sheath nanomatchsticks for non-enzymatic glucose biosensor. *Nano. Res.* **2023**, *16*, 1558-67. DOI
77. Zhong, Y.; Kong, X.; Song, Z.; et al. Adjusting local CO confinement in porous-shell Ag@Cu catalysts for enhancing C-C coupling toward CO_2 eletroreduction. *Nano. Lett.* **2022**, *22*, 2554-60. DOI
78. Zhang, S.; Zhao, S.; Qu, D.; et al. Electrochemical reduction of CO_2 Toward C_2 valuables on Cu@Ag core-shell tandem catalyst with tunable shell thickness. *Small* **2021**, *17*, e2102293. DOI
79. Wu, X.; Tian, X.; Jiang, Z.; et al. Engineering the inter-island plasmonic coupling in homometallic Au-Aun core-satellite structures. *Nano. Res.* **2023**, *16*, 10690-7. DOI
80. Yin, Z.; Wang, Y.; Song, C.; et al. Hybrid Au-Ag nanostructures for enhanced plasmon-driven catalytic selective hydrogenation through visible light irradiation and surface-enhanced Raman scattering. *J. Am. Chem. Soc.* **2018**, *140*, 864-7. DOI
81. Yang, Y.; Zhu, J.; Zhao, J.; Weng, G. J.; Li, J. J.; Zhao, J. W. Growth of spherical gold satellites on the surface of Au@Ag@SiO_2 core-shell nanostructures used for an ultrasensitive SERS immunoassay of alpha-fetoprotein. *ACS. Appl. Mater. Interfaces.* **2019**, *11*, 3617-26. DOI
82. Zhang, X.; Fu, Q.; Duan, H.; Song, J.; Yang, H. Janus nanoparticles: from fabrication to (bio)applications. *ACS. Nano.* **2021**, *15*, 6147-91. DOI
83. Xu, Y.; Shi, L.; Jing, X.; Miao, H.; Zhao, Y. SERS-active composites with Au-Ag Janus nanoparticles/perovskite in immunoassays for staphylococcus aureus enterotoxins. *ACS. Appl. Mater. Interfaces.* **2022**, *14*, 3293-301. DOI
84. Woessner, Z. J.; Skrabalak, S. E. Symmetry-reduced metal nanostructures offer new opportunities in plasmonics and catalysis. *J. Phys. Chem. C.* **2021**, *125*, 23587-96. DOI
85. Agrawal, G.; Agrawal, R. Janus nanoparticles: recent advances in their interfacial and biomedical applications. *ACS. Appl. Nano. Mater.* **2019**, *2*, 1738-57. DOI
86. Qiu, J.; Xie, M.; Lyu, Z.; Gilroy, K. D.; Liu, H.; Xia, Y. General approach to the synthesis of heterodimers of metal nanoparticles through site-selected protection and growth. *Nano. Lett.* **2019**, *19*, 6703-8. DOI
87. Feng, J.; Yang, F.; Wang, X.; Lyu, F.; Li, Z.; Yin, Y. Self-aligned anisotropic plasmonic nanostructures. *Adv. Mater.* **2019**, *31*, e1900789. DOI
88. Wang, J.; Luo, D.; Cai, Y.; Li, X. L.; Chen, H. Y.; Xu, J. J. A plasmonic Au-Ag janus nanoprobe for monitoring endogenous hydrogen sulfide generation in living cells. *Biosens. Bioelectron.* **2022**, *213*, 114422. DOI
89. Xu, Y.; Jin, Z.; Zhao, Y. Tunable preparation of SERS-active Au-Ag Janus@Au NPs for label-free staphylococcal enterotoxin C detection. *J. Agric. Food. Chem.* **2023**, *71*, 1224-33. DOI
90. Zeng, P.; Hang, L.; Zhang, G.; et al. Atom absorption energy directed symmetry-breaking synthesis of Au-Ag hierarchical nanostructures and their efficient photothermal conversion. *Small* **2022**, *18*, e2204748. DOI
91. Wu, G. F.; Zhu, J.; Weng, G. J.; Cai, H. Y.; Li, J. J.; Zhao, J. W. Morphology and optical properties of Au-Ag hybrid nanoparticles regulation and its ultra-sensitive SERS immunoassay detection in carbohydrate antigen 19-9. *Talanta* **2024**, *275*, 126131. DOI PubMed

92. Fan, X.; An, S.; Jia, J.; et al. Tuning Au-Cu Janus structures through strong ligand-mediated interfacial energy control. *Chem. Mater.* **2022**, *34*, 6057-67. DOI
93. Zhang, T.; Zhang, B.; Zang, Y.; Zeng, P.; Li, Y.; Fan, H. J. A selectivity switch for CO_2 electroreduction by continuously tuned semi-coherent interface. *Chem* **2024**, *10*, 2745-60. DOI
94. Huang, J.; Mensi, M.; Oveisi, E.; Mantella, V.; Buonsanti, R. Structural sensitivities in bimetallic catalysts for electrochemical CO_2 reduction revealed by Ag-Cu nanodimers. *J. Am. Chem. Soc.* **2019**, *141*, 2490-9. DOI PubMed
95. Ma, Y.; Yu, J.; Sun, M.; et al. Confined growth of silver-copper Janus nanostructures with {100} facets for highly selective tandem electrocatalytic carbon dioxide reduction. *Adv. Mater.* **2022**, *34*, e2110607. DOI
96. Fleischmann, M.; Hendra, P.; Mcquillan, A. Raman spectra of pyridine adsorbed at a silver electrode. *Chem. Phys. Lett.* **1974**, *26*, 163-6. DOI
97. Dong, S.; He, D.; Zhang, Q.; et al. Early cancer detection by serum biomolecular fingerprinting spectroscopy with machine learning. *eLight* **2023**, *3*, 51. DOI
98. Arabi, M.; Ostovan, A.; Wang, Y.; et al. Chiral molecular imprinting-based SERS detection strategy for absolute enantiomeric discrimination. *Nat. Commun.* **2022**, *13*, 5757. DOI PubMed PMC
99. Hu, J.; Chen, G. J.; Xue, C.; et al. RSPSSL: a novel high-fidelity Raman spectral preprocessing scheme to enhance biomedical applications and chemical resolution visualization. *Light. Sci. Appl.* **2024**, *13*, 52. DOI PubMed PMC
100. Wang, X.; Hou, J.; Chen, C.; et al. Non-invasive detection of systemic lupus erythematosus using SERS serum detection technology and deep learning algorithms. *Spectrochim. Acta. A. Mol. Biomol. Spectrosc.* **2024**, *320*, 124592. DOI
101. Yang, J.; Chen, X.; Luo, C.; et al. Application of serum SERS technology combined with deep learning algorithm in the rapid diagnosis of immune diseases and chronic kidney disease. *Sci. Rep.* **2023**, *13*, 15719. DOI PubMed PMC
102. Chen, J.; Hu, J.; Xue, C.; et al. Combined mutual learning net for raman spectral microbial strain identification. *Anal. Chem.* **2024**, *96*, 5824-31. DOI
103. Yi, L.; Zhang, J.; Wu, J.; et al. Micro-macro SERS strategy for highly sensitive paper cartridge with trace-level molecular detection. *Biosens. Bioelectron.* **2024**, *264*, 116665. DOI
104. Cardellini, J.; Dallari, C.; De, S. I.; et al. Hybrid lipid-AuNP clusters as highly efficient SERS substrates for biomedical applications. *Nat. Commun.* **2024**, *15*, 7975. DOI PubMed PMC
105. Hopper, E. R.; Boukouvala, C.; Asselin, J.; Biggins, J. S.; Ringe, E. Opportunities and challenges for alternative nanoplasmonic metals: magnesium and beyond. *J. Phys. Chem. C. Nanomater. Interfaces.* **2022**, *126*, 10630-43. DOI PubMed PMC
106. Jiang, N.; Zhuo, X.; Wang, J. Active plasmonics: principles, structures, and applications. *Chem. Rev.* **2018**, *118*, 3054-99. DOI
107. Li, J. F.; Zhang, Y. J.; Ding, S. Y.; Panneerselvam, R.; Tian, Z. Q. Core-shell nanoparticle-enhanced Raman spectroscopy. *Chem. Rev.* **2017**, *117*, 5002-69. DOI PubMed
108. Yang, Y.; Liu, J.; Fu, Z. W.; Qin, D. Galvanic replacement-free deposition of Au on Ag for core-shell nanocubes with enhanced chemical stability and SERS activity. *J. Am. Chem. Soc.* **2014**, *136*, 8153-6. DOI
109. Du, H. F.; Zhu, J.; Weng, G. J.; Li, J. J.; Li, X.; Zhao, J. W. Site-selective growth and plasmonic spectral properties of L-shaped Janus Au-Ag gold nanodumbbells for surface-enhanced Raman scattering. *Spectrochim. Acta. A. Mol. Biomol. Spectrosc.* **2023**, *299*, 122862. DOI
110. Hao, H. L.; Zhu, J.; Weng, G. J.; Li, J. J.; Guo, Y. B.; Zhao, J. W. Exclusive core-Janus satellite assembly based on Au-Ag Janus self-aligned distributions with abundant hotspots for ultrasensitive detection of CA19-9. *ACS. Sens.* **2024**, *9*, 942-54. DOI PubMed
111. Zhang, W.; Liu, J.; Niu, W.; Yan, H.; Lu, X.; Liu, B. Tip-selective growth of silver on gold nanostars for surface-enhanced Raman scattering. *ACS. Appl. Mater. Interfaces.* **2018**, *10*, 14850-6. DOI
112. Wang, Z.; Zhou, Y.; Wang, J.; et al. Site-specific growth of Ag islands on concave Au nanocubes for SERS and LSPR-based applications. *ACS. Appl. Nano. Mater.* **2024**, *7*, 22002-10. DOI
113. Eustis, S.; El-Sayed, M. A. Why gold nanoparticles are more precious than pretty gold: noble metal surface plasmon resonance and its enhancement of the radiative and nonradiative properties of nanocrystals of different shapes. *Chem. Soc. Rev.* **2006**, *35*, 209-17. DOI PubMed
114. Zhao, X.; Wang, J.; Jia, Y. Block copolymer-templated surface-enhanced Raman scattering-active nanofibers for hydrogen sulfide detection. *Talanta* **2024**, *270*, 125608. DOI
115. Gandra, N.; Abbas, A.; Tian, L.; Singamaneni, S. Plasmonic planet-satellite analogues: hierarchical self-assembly of gold nanostructures. *Nano. Lett.* **2012**, *12*, 2645-51. DOI PubMed
116. Le, T.; Vo, T.; Gwon, Y.; Lee, H.; Lee, S. Fiber-optic sensing system using polyhedral plasmonic nanostructures as SERS-active substrates. *ACS. Appl. Nano. Mater.* **2024**, *7*, 21114-23. DOI
117. Ding, Z.; Wang, P.; Li, Z.; Guo, Y.; Ma, Q. Sulfur dots/Au@Ag nanorods array-based polarized ECL sensor for the detection of thyroid cancer biomarker. *Talanta* **2023**, *265*, 124925. DOI
118. Zhao, C. Q.; Zhou, J.; Wu, K. W.; Ding, S. N.; Xu, J. J.; Chen, H. Y. Plasmonic enhanced gold nanoclusters-based photoelectrochemical biosensor for sensitive alkaline phosphatase activity analysis. *Anal. Chem.* **2020**, *92*, 6886-92. DOI PubMed
119. Zhang, W. S.; Wang, Y. N.; Xu, Z. R. High sensitivity and non-background SERS detection of endogenous hydrogen sulfide in living cells using core-shell nanoparticles. *Anal. Chim. Acta.* **2020**, *1094*, 106-12. DOI PubMed
120. Zhu, X.; Zhuo, X.; Li, Q.; Yang, Z.; Wang, J. Gold nanobipyramid-supported silver nanostructures with narrow plasmon linewidths and improved chemical stability. *Adv. Funct. Mater.* **2016**, *26*, 341-52. DOI

121. He, Z.; Zhu, J.; Li, X.; Weng, G. J.; Li, J. J.; Zhao, J. W. Au@Ag nanopencil with Au tip and Au@Ag rod: multimodality plasmonic nanoprobe based on asymmetric etching for the detection of SCN^- and ClO^-. *Small* **2023**, *19*, e2302302. DOI
122. Brongersma, M. L.; Halas, N. J.; Nordlander, P. Plasmon-induced hot carrier science and technology. *Nat. Nanotechnol.* **2015**, *10*, 25-34. DOI PubMed
123. Lee, H.; Park, Y.; Song, K.; Park, J. Y. Surface plasmon-induced hot carriers: generation, detection, and applications. *Acc. Chem. Res.* **2022**, *55*, 3727-37. DOI
124. DuChene, J. S.; Tagliabue, G.; Welch, A. J.; Cheng, W. H.; Atwater, H. A. Hot hole collection and photoelectrochemical CO_2 reduction with plasmonic Au/p-GaN photocathodes. *Nano. Lett.* **2018**, *18*, 2545-50. DOI PubMed
125. Song, K.; Lee, H.; Lee, M.; Park, J. Y. Plasmonic hot hole-driven water splitting on Au nanoprisms/P-type GaN. *ACS. Energy. Lett.* **2021**, *6*, 1333-9. DOI
126. Corson, E. R.; Subramani, A.; Cooper, J. K.; Kostecki, R.; Urban, J. J.; McCloskey, B. D. Reduction of carbon dioxide at a plasmonically active copper-silver cathode. *Chem. Commun.* **2020**, *56*, 9970-3. DOI